Agricultural and Forest Meteorology 368 (2025) 110526

Contents lists available at ScienceDirect

Agricultural and Forest Meteorology

journal homepage: www.elsevier.com/locate/agrformet

Incorporation of needleleaf traits improves estimation of light absorption and gross primary production of evergreen needleleaf forests

Baihong Pan [a], Xiangming Xiao [a,*], Li Pan [a], Cheng Meng [a], Peter D. Blanken [b], Sean P. Burns [b,c], Jorge A. Celis [a], Chenchen Zhang [a], Yuanwei Qin [a]

[a] School of Biological Sciences, Center for Earth Observation and Modeling, University of Oklahoma, 101 David L. Boren Blvd., Norman, OK 73019, USA
[b] Department of Geography, University of Colorado, Boulder, CO 80309, USA
[c] National Center for Atmospheric Research, Boulder, CO 80305, USA

ARTICLE INFO

Keywords:
GPP
Vegetation photosynthesis model
ENF
$FPAR_{chl}$

ABSTRACT

The seasonal dynamics and interannual variation of gross primary production (GPP, g C/m^2/day) of evergreen needleleaf forest (ENF) are important but most of models underestimate ENF GPP. In this work, we selected three ENF sites with 10+ years of data from the eddy flux towers and investigated temporal dynamics of GPP, climate, and vegetation greenness (as measured by vegetation indices from MODIS surface reflectance data) during 2000–2020. We found that the seasonal dynamics of GPP and vegetation indices were correlated highly at two sites (US-Ho2, US-NR1) under Warm Summer Continental climate (Dfb) and Subarctic climate (Dfc), where the seasonality of air temperature, radiation and rainfall are synchronized, but weakly at the site (US-Me2) under Mediterranean climate (Csb), where the seasonality of air temperature and radiation is asynchronized with that of rainfall and trees have deep roots for access to deep soil water in a year. We incorporated the needleleaf traits and modified the equation that estimates light absorption by chlorophyll of needleleaf in the data-driven Vegetation Photosynthesis Model (VPM), which resulted in substantial improvement of GPP estimates. Daily GPP estimates over 2000–2020 from the VPM (v3.0) agreed well with the GPP estimates provided by AmeriFlux. As ENF at the US-Me2 site under the Mediterranean climate has deep roots for access water in the deep soils, we incorporated no-water stress in the wet season for the VPM (v3.0) simulations, which further improved GPP estimates of ENF at the site. This study highlights the importance of needleleaf traits and plant root traits in the VPM v3.0 for estimating GPP of evergreen needleleaf forests under different types of climate systems.

1. Introduction

The exchange of carbon dioxide (CO_2) between the land and the atmosphere is fundamental to the carbon cycle (Green et al., 2019; Knutti et al. 2017). The carbon sequestration potential via photosynthesis of evergreen needleleaf forests (ENFs) is high, with an uptake of approximately 2 billion tons of carbon dioxide per year (Keenan et al. 2015). At the ecosystem scale, the eddy covariance method has been used to measure net CO_2 exchange between the land and the atmosphere at various sites (Baldocchi 2020). Eddy flux towers in evergreen needleleaf forests provide comprehensive flux measurements over areas ranging from a few to many hectares, depending on the tower height and weather conditions (Xiao et al. 2004). The data from the flux towers are limited to local areas, and researchers use these data to develop and evaluate models, including process-based models (Smallman and Williams 2019; Vinukollu et al. 2011) and data-driven models (Jung et al. 2020; Wagle et al. 2016).

Many models are driven by remote sensing data and provide time series data of gross primary production (GPP) across the scales from local to the globe (Junttila et al. 2023; Pierrat et al. 2022). Some of these models use reflectance-based vegetation indices such as the Normalized Difference Vegetation Index (NDVI), the near-infrared reflectance of vegetation index (NIR_V) and the Enhanced Vegetation Index (EVI), which are widely used for monitoring canopy greenness and structure (Huang et al. 2019; Zeng et al. 2022). NDVI is less effective in ENFs due to the limited seasonal variation in canopy greenness and structure (Tucker 1979; Wang et al. 2023). The NIR_V is considered as a good proxy for daily GPP in ENFs (Wong et al. 2020), as it effectively tracks seasonal GPP dynamics by capturing vegetation light absorption influenced by greenness, leaf area, orientation, and canopy structure (Badgley et al.

* Corresponding author.
E-mail address: xiangming.xiao@ou.edu (X. Xiao).

https://doi.org/10.1016/j.agrformet.2025.110526
Received 19 January 2025; Received in revised form 19 March 2025; Accepted 25 March 2025
Available online 16 April 2025

2019). EVI is closely related to leaf and canopy chlorophyll content and the fraction of light absorbed by chlorophyll in leaf and canopy of forests (Zhang et al. 2005; Zhang et al. 2006) and has strong linear relationship with GPP (Xiao et al. 2004). As the Photochemical Reflectance Index (PRI) is sensitive to xanthophyll pigment activity and modulates thermal energy dissipation, some models use PRI for tracking photosynthetic phenology (Gamon et al. 1992; Wong and Gamon 2015). The chlorophyll-carotenoid index (CCI), the satellite proxy for PRI, was designed to track the seasonal dynamics of the chlorophyll-to-carotenoid ratio, which makes it an effective proxy for ENF carbon uptake (Gamon et al. 2016). In recent years, solar-induced chlorophyll fluorescence (SIF) has shown significant potential for tracking GPP of ENF, which is then used as a robust proxy for photosynthesis even in the presence of snow and cloud cover (Kim et al. 2021). At present, satellite-based SIF measurements have coarse spatial resolution and require complex instruments for accurate measurement of SIF (Mohammed et al. 2019).

The light use efficiency (LUE) models estimate GPP by multiplying the energy absorbed by plants with the actual LUE that converts energy to carbon fixed during the Calvin cycle (Monteith 1972). These LUE models can be driven by remote sensing vegetation index data, which are globally available at various spatial resolutions (Huang et al. 2021; Pei et al. 2022). Several LUE models have been developed, for example, the MOD17 model (Running and Zhao 2015), the eddy covariance (EC-LUE) model (Yuan et al. 2007; Zheng et al. 2020), the Carnegie-Ames-Stanford Approach (CASA) (Cao et al. 2016; Potter et al. 1993), and the Vegetation Photosynthesis Model (VPM) (Xiao et al. 2005a; Zhang et al. 2017). The EVI-driven VPM has demonstrated its ability to simulate GPP of forests (Xiao et al. 2004; Xiao et al. 2005a; Zhang et al. 2016). EVI captures the changes in chlorophyll content within evergreen leaves and reflects canopy-level structural changes (leaf area index, plant area index), even though they only change moderately over the growing season (Xiao et al. 2005b).

In this study we investigated the seasonal dynamics and interannual variation of carbon fluxes over three evergreen needleleaf forest sites under varying climate and soil water conditions, which has 10+ years of data from the eddy flux tower systems. Note that although there are many ENF sites in the AmeriFlux and Fluxnet, few of them have 10+ years of data. We developed and evaluated the performance of a new version of VPM (VPM v3.0) in estimating GPP at the three sites. By integrating remote sensing and eddy flux tower data, our study addressed three major questions: (1) What are the ranges of inter-annual variation of ENF GPP over 10+ years? (2) How to incorporate needleleaf traits to improve estimation of light absorption by needleleaf and then GPP estimates of ENF in the VPM v3.0 model? and (3) how to incorporate the deep roots of ENF under the Mediterranean climate, which enables its access to deep soil water in the site, to assess the effect of water stress and improve GPP estimates of ENF in the VPM v3.0 model? This study could help us to better understand interannual variation of GPP over 10+ years and improve and evaluate VPM v3.0 for estimating daily GPP of evergreen needleleaf forests over years.

2. Materials and methods

2.1. Study area

We chose three ENF sites in the AmeriFlux based on three criteria: (1) availability of 20+ years of observational records, with usable data filtered to 10+ years (Table 1); (2) a minimum of 60 % coverage by ENF within the 500-m MODIS pixel that encompasses the eddy flux tower location (Fig. 1); and (3) a predominance of ENF within approximately an area of 1-km^2 surrounding the eddy flux tower. In specific, among the

Table 1
Overview of characteristics for three ENF eddy flux tower sites. MAP - mean annual precipitation (mm); MAT - mean annual air temperature (°C); LAI - leaf area index (m^2/m^2).

Sites Variables		US-Ho2	US-NR1	US-Me2
Geolocation (latitude, longitude, elevation a.s.l.)		(45.2091°, −68.7470°, 61-m)	(40.0329°, −105.5464°, 3050-m)	(44.4523°, −121.5574°, 1253-m)
Climate	Type	Warm Summer Continental	Subarctic	Mediterranean
	MAP(mm)	1064	800	523
	MAT(°C)	5.1	1.5	6.3
Soil	Type	Loamy sand	Loamy sand	Sandy
	Access to deep soil water	/	/	Yes
Vegetation and leaf traits	Major tree species	Red spruce and eastern hemlock	Subalpine fir, Engelmann spruce and lodgepole pine	Ponderosa pine
	Peak LAI (m^2/m^2)	5	4.2	2.8
	Forest stand ages	Mean age ≈ 120y	Varied from 80 to 120y	Mean age ≈ 71y
Data period		2007–2020	2000–2016	2002–2019
Reference		(Davidson et al. 2006; Richardson et al. 2019; Xiao et al. 2005a)	(Burns et al. 2015; Knowles et al. 2020)	(Law 2022; Law et al. 2001; Still et al. 2021; Thomas et al. 2009)

Fig. 1. Geographic positions and adjacent areas of three evergreen needleleaf forest sites. The light blue polygon represents the area covered by a MODIS pixel with a spatial resolution of 500 m The red dot represents the location of the flux tower. (a) US-Ho2 site, (b) US-NR1 site, and (c) US-Me2 site.

54 ENF sites in the "AmeriFlux FLUXNET Data", only six sites met the criteria of having 20+ years of observational records. From these six, we selected Howland Forest site (West Tower, US-Ho2), Niwot Ridge Forest site (Long Term Ecological Research, NWT1, US-NR1), and Metolius Mature Ponderosa Pine site (US-Me2). These sites were chosen to represent three distinct temperate climate systems: Warm Summer Continental, Subarctic (located in a mid-latitude mountainous region), and Mediterranean climates, respectively. Other sites with similar climates were excluded. Table 1 contains a concise overview of these three ENF sites.

2.2. Datasets

2.2.1. In-situ data from the eddy flux tower sites

We used half-hourly meteorological and GPP data provided by the AmeriFlux dataset (https://ameriflux.lbl.gov/data/flux-data-products/). The meteorological data include incoming photosynthetic photon flux density (PPFD_IN), air temperature (T_{EC}), precipitation (P_{EC}) and soil water content (SWC_{EC}). We used GPP_{EC}, which was estimated by the method that partitions daytime NEE data into GPP and ecosystem respiration (ER) (NEE = GPP - ER) (Lasslop et al. 2009). In this method, both the GPP and ER are estimated simultaneously by the model.

We calculated the photosynthetically active radiation (PAR_{EC}) from PPFD_IN (Eq. (1)):

$$PAR_{EC} = PPFD\_IN \times 10^{-6} \times 60 \times 30 \quad (1)$$

Here, PPFD_IN is in the unit of μmol m^{-2} s^{-1}. The formula converts PPFD_IN to PAR_{EC} over 30 min, resulting in the unit of mol m^{-2} per half-hour, accounting for the conversion from micromoles to moles and aggregation over a half-hour. In this study we used the daytime data, following the same procedure used in previous publication (Chang et al. 2021). For simplicity, the daytime period is delineated by PAR_{EC} greater than 0 (Ogle et al. 2012). We averaged the half-hourly T_{EC} with PAR_{EC} greater than 0 to calculate the daily daytime air temperature ($T_{EC\text{-}DT}$). We summed the half-hourly PAR_{EC} and the GPP_{EC} respectively during the daytime as the daily daytime data. We calculated the averages of the half-hourly SWC_{EC}, and sums of the half-hourly P_{EC} as the daily data. For each of these variables, we calculated an average at eight-day interval, aligning with the MODIS temporal resolution.

2.2.2. MODIS land surface reflectance and vegetation indices during 2000–2020

We used the Moderate Resolution Imaging Spectroradiometer (MODIS) surface reflectance product (MOD09A1 V6.1), which has seven spectral bands (1–7), covering wavelengths from 0.459 μm to 2.155 μm (Vermote 2015). The MOD09A1 dataset has a spatial resolution of 500 m and an 8-day temporal resolution, and has been atmospherically corrected to account for gases, aerosols, and Rayleigh scattering. We used surface reflectance state flags (StateQA) of MOD09A1 V6.1 to identify bad-quality observations affected by cloud (Fig. 2). The bad-quality observations for the US-Ho2 and US-NR1 sites were mainly concentrated in the winter season (snow season). The data analyses are thus focused on the snow-free periods at the US-Ho2 and US-NR1 sites. During May through October, approximately 92 % of observations are classified as good quality at the US-Ho2 and US-NR1 sites (see calculation of snow-free seasons see Section 2.3.1). The data analyses used data over the entire year at the US-Me2 site, where on the average 88 % of the observations are good-quality observations.

For the time series data, we gap-filled the bad-quality observations with the linear interpolation method. After pre-processing MOD09A1 V6.1 data, red (RED) (620–670 nm), blue (BLUE) (459–479 nm), near infrared (NIR) (841–876 nm) and short wavelength near infrared (SWIR) (1628–1652 nm) were used to calculate three vegetation indices (Table 2): (1) Normalized Difference Vegetation Index (NDVI; (Tucker 1979)), (2) Enhanced Vegetation Index (EVI; (Huete et al. 2002)), and (3) Land Surface Water Index (LSWI; (Xiao et al. 2002)).

Since the flux towers may be situated on the edges of MODIS pixels, we evaluated all MODIS pixels within a 500-meter radius centered on each tower (Fig. 3). This 500-meter radius was selected based on previous research showing that the daytime footprints of the three sites fall within this range (Chu et al. 2021). Using EVI as an example, the EVI from the pixel containing the flux tower closely aligns with the average EVI of all selected MODIS pixels (Fig. 3). Therefore, for simplicity and consistency with the procedure reported in previous work (Xiao et al., 2005), the MODIS pixel with the tower is used for data analyses in this study.

2.2.3. Climate data from the fifth generation ECMWF atmospheric reanalysis dataset (ERA5)

ERA5-Land dataset is a reanalysis climate dataset and provides a consistent representation of land variables over time at fine spatial resolution (9-km grid spacing) (Muñoz Sabater 2019). It is produced by the ECMWF ERA5 climate reanalysis and ERA-Land uses ERA5 atmospheric variables (e.g., air temperature, humidity, pressure) as input to control the simulated land fields. We used the ERA5-Land hourly dataset (Muñoz-Sabater et al. 2021) as input data for simulations of VPM from 2000 to 2020. The hourly downward surface solar radiation (SW_IN) was summed to generate daily daytime data, and then averaged over 8-day period to match the model simulation interval. SW_IN was used to calculate the PAR_{ERA5} (Eq. (2)).

$$PAR_{ERA5} = SW\_IN \times f_{PAR} \times \beta \quad (2)$$

where SW_IN (J/m^2) represents the incoming shortwave radiation from the ERA5 dataset; $f_{PAR} = 0.45$ indicates the portion of PAR relative to SW (Ma et al. 2014; Meek et al. 1984), $\beta = 4.56$ μmol J^{-1} is the conversion factor for energy to quanta (Dye 2004). The hourly air temperature (°C) during the daytime (defined as PAR_{ERA5} greater than 0) was averaged to generate daily daytime data, and then averaged over each 8-day period to generate $T_{DT\text{-}ERA5}$.

The relationships between climate data from ERA5 (PAR_{ERA5}, $T_{DT\text{-}ERA5}$) and those observed at the flux tower sites (PAR_{EC}, $T_{DT\text{-}EC}$) during the whole year were plotted for each site (Fig. 4). PAR_{ERA5} was highly correlated with PAR_{EC} (R^2 value > 0.91), and the slope values for a regression line between PAR_{ERA5} and PAR_{EC} were small at the US-Ho2 (3 %) site, moderate at US-Me2 (6 %) site, but large at the US-NR1 (28 %) site, which may be related to local complex topography (Urraca et al. 2018). $T_{DT\text{-}ERA5}$ was also highly correlated with $T_{DT\text{-}EC}$ ($R^2 > 0.94$), and the slope value for a regression line between $T_{DT\text{-}ERA5}$ and $T_{DT\text{-}EC}$ ranged from moderate (8 %) to large (21 %), which was consistent with an earlier study showing R^2 between PAR_{ERA5} ($T_{DT\text{-}ERA5}$) and PAR_{EC}

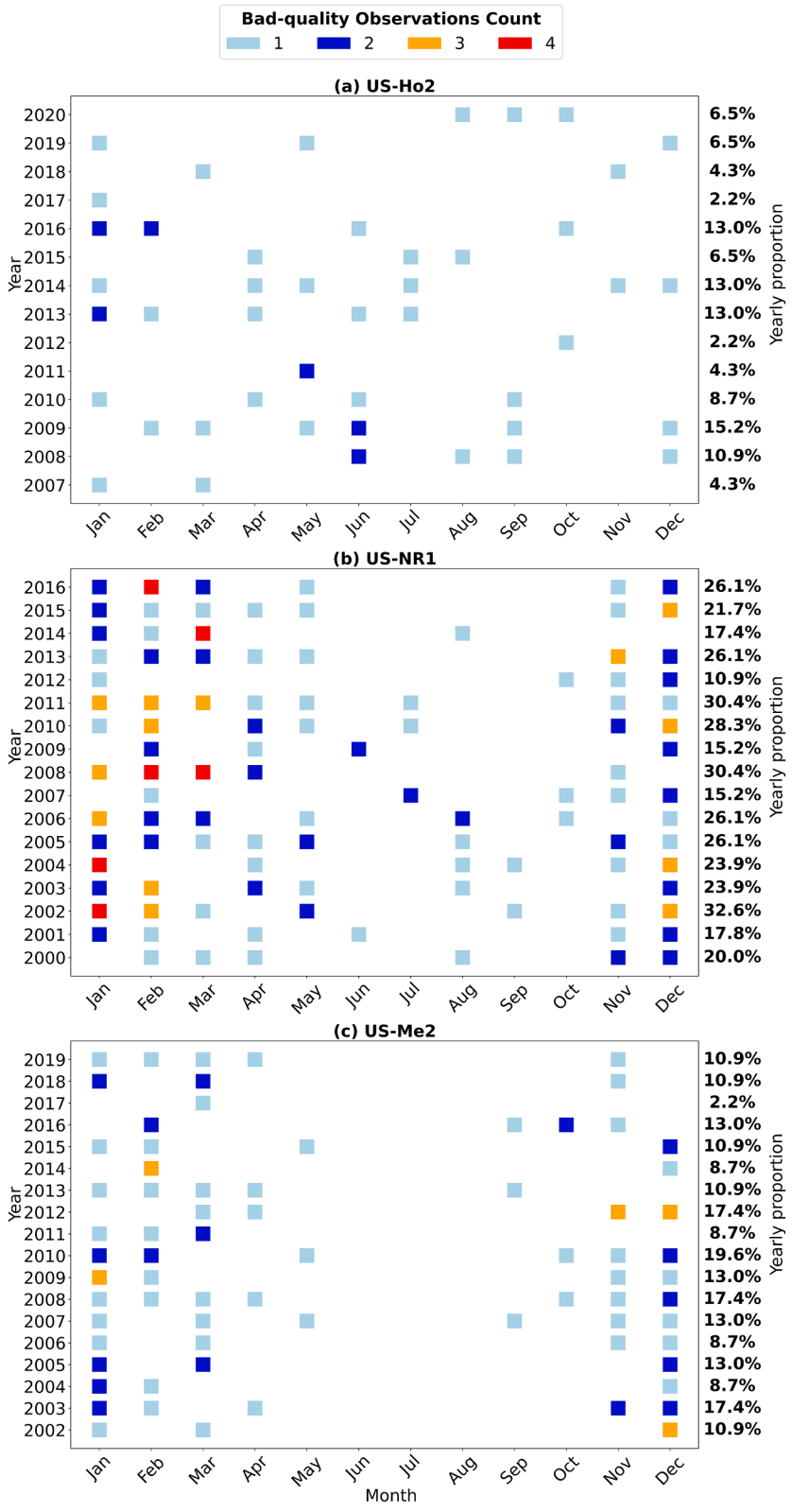

Fig. 2. Annual bad-quality observations labeled as cloud-affected by StateQA: monthly counts and yearly proportions (shown at each subfigure's far right). (a) US-Ho2, 2007–2020; (b) US-NR1, 2000–2016; (c) US-Me2, 2002–2019.

Table 2
Vegetation indices.

Index	Formula	Description
NDVI	$NDVI = \frac{NIR - RED}{NIR + RED}$	Related to green leaf area index (LAI), often used to assess vegetation density and health.
EVI	$EVI = 2.5 \times \frac{NIR - RED}{(NIR + 6 \times RED - 7.5 \times BLUE + 1)}$	Related not only to LAI but also sensitive to chlorophyll content and leaf age, providing enhanced monitoring of canopy variations and reducing atmospheric effects.
LSWI	$LSWI = \frac{NIR - SWIR}{NIR + SWIR}$	Useful for assessing water content in vegetation and soil moisture; used for evaluation of moisture stress and drought conditions.

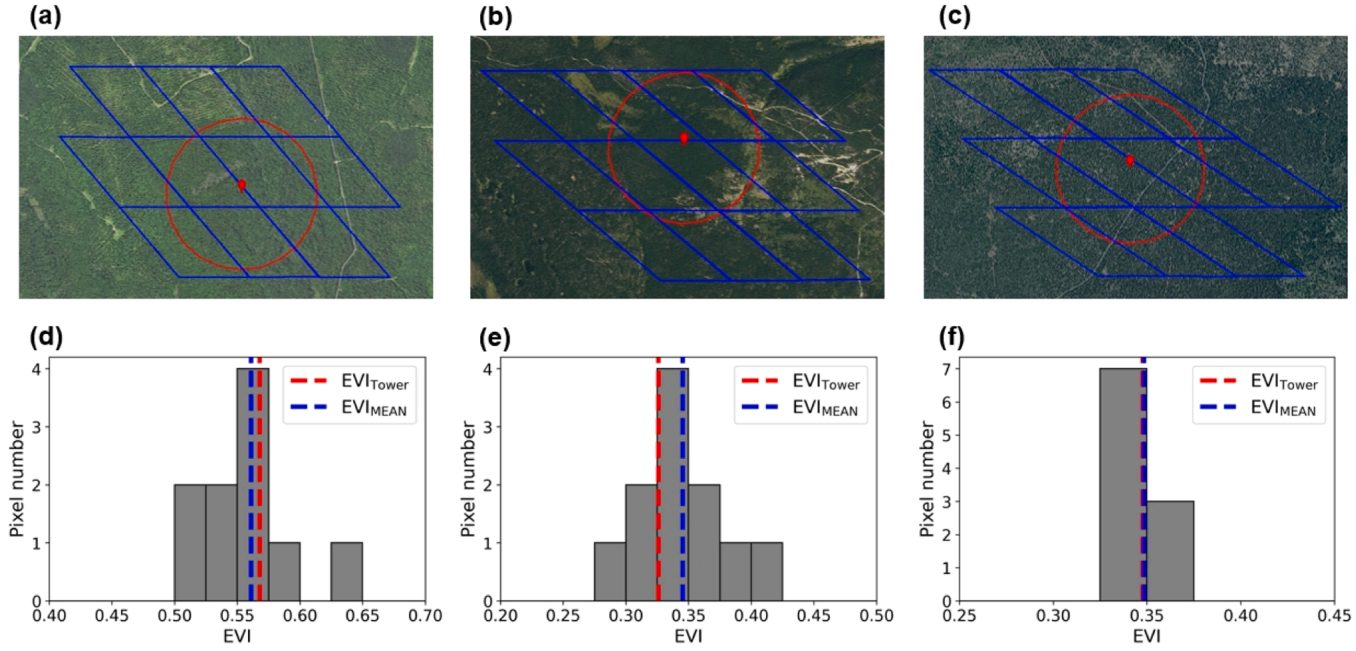

Fig. 3. Distribution of EVI values in the footprint of each flux site. Figures (a) to (c) are the footprint of each flux site (Red circle with a radius of 500 m) and the 500-m MODIS pixels (Blue polygon) intersecting this circle. Figures (d) to (f) are the histograms of EVI for the MODIS pixels of the three flux towers, using data from July 20, 2010 as an example. The red dot line indicates the EVI of the pixel where the tower is located (EVI_{Tower}, which is utilized as an input in VPM v3.0). The blue dot line indicates the mean EVI of all the pixels (EVI_{MEAN}).

($T_{DT\text{-}EC}$) higher than 0.7 in 90 % of 204 sites in FLUXNET 2015 (Zeng et al. 2020).

2.2.4. The snow-free season and active growing season at the individual sites

As snow affects surface reflectance and vegetation indices, we delineated the snow-free season and our data analyses focused on observations within the snow-free season. which is defined by daytime mean air temperature at the EC tower sites ($T_{DT\text{-}EC}$) (Chang et al. 2019). The start of the snow-free season was defined as the third date of three consecutive 8-day observations with $T_{DT\text{-}EC}$ above 5 °C, and the end of the snow-free season date was defined as the date before three consecutive 8-day observations with $T_{DT\text{-}EC}$ below 5 °C (Chang et al. 2021). We further selected observations with $T_{DT\text{-}EC}$ greater than 5 °C in the above time period to avoid the effects from possible temperature dips in the spring (Gu et al. 2008). We delineated the snow-free season for each site-year at the three ENF sites by $T_{DT\text{-}EC}$ and $T_{DT\text{-}ERA5}$ respectively. The data within the snow-free season were used to estimate site-specific apparent optimum air temperature for photosynthesis ($T_{opt\text{-}site}$), which is then used for VPM simulation.

For comparison between predicted GPP from model simulations and GPP from the eddy flux tower sites, we delineated the active growing season by using air temperature and vegetation productivity as an indicator for the "active growing season" (Korner et al. 2023; Liu et al. 2016; Yuan et al. 2018). The sites were divided into two groups according to their winter climate: (1) US-Ho2 and US-NR1, where ENF experiences dormancy every year during the cold winter (Havranek and Tranquillini 1995; Knowles et al. 2020), and (2) US-Me2, where ENF experiences different winter conditions, including some years characterized by cold winters resulting in ENF dormancy and other years marked by warm winters conducive to regular ENF growth. For the US-Ho2 and US-NR1 sites, we delineated the period between the first observation with $T_{DT\text{-}EC}$ above −1 °C and the last observation with $T_{DT\text{-}EC}$ above −1 °C in each year, as −1 °C is considered as the minimum air temperature threshold value (T_{min}) for photosynthesis of ENFs in some ecosystem models (Zhang et al. 2017). We used GPP_{EC} larger than 1 g C/m^2/day to delineate the start of the active growing season (SOS) and GPP_{EC} lower than 1 g C/m^2/day at the next 8-day observation as the end of the growing season (EOS) (Xin et al. 2017). We further selected observations with $T_{DT\text{-}EC}$ greater than −1 °C in the above active growing season. For the US-Me2 site, we selected observations from whole year with $T_{DT\text{-}EC}$ above −1 °C and GPP_{EC} above 1 g C/m^2/day as the active growth season. We did not delineate the SOS and EOS at the US-Me2 site because it has both warm and cold winters varying from year to year and photosynthesis can start at any time as long as the air temperatures are favorable.

2.3. Vegetation photosynthesis model (VPM)

The VPM estimates daily GPP (g C/m^2/day) as the product of light

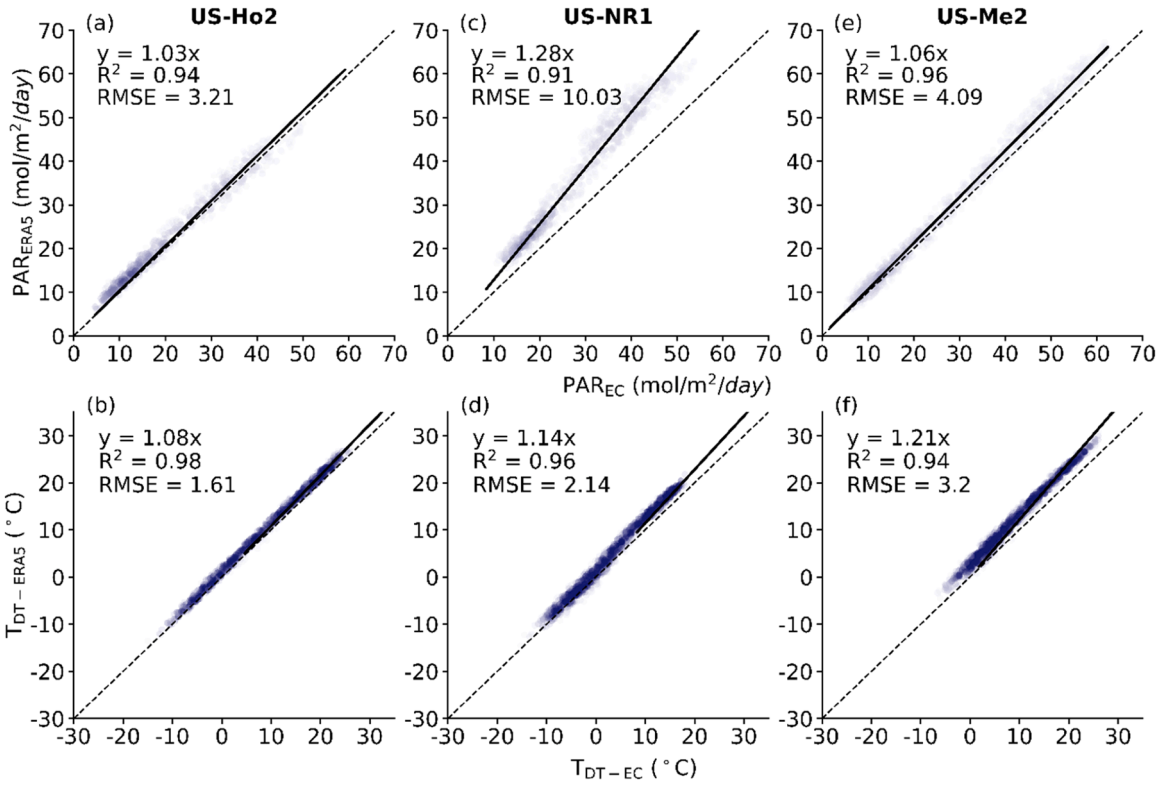

Fig. 4. The relationships between climate data obtained by ERA5 and observed by flux tower during the whole year. (a~b) US-Ho2, 2007–2020; (c~d) US-NR1, 2000–2016; (e~f) US-Me2, 2002–2019. The darker the color of the scatterplot, the more dots there are.

absorption by chlorophyll in the canopy ($APAR_{chl}$) and the light use efficiency (ε_g):

$$GPP = APAR_{chl} \times \varepsilon_g \quad (3)$$

$APAR_{chl}$ is calculated as a product of photosynthetically active radiation (PAR) and the fraction of PAR absorbed by chlorophyll ($FPAR_{chl}$):

$$APAR_{chl} = FPAR_{chl} \times PAR \quad (4)$$

The $FPAR_{chl}$ is calculated as a linear function of EVI (Zhang et al. 2016; Zhang et al. 2017).

ε_g in Eq. (5) is downregulated by air temperature limitation (T_{scalar}) and water stress (W_{scalar}) from its maximum value (ε_0):

$$\varepsilon_g = \varepsilon_0 \times T_{scalar} \times W_{scalar} \quad (5)$$

where ε_0 differs by plant function types (C3 vs C4 plants) (Wang et al. 2016; Xiao 2004).

2.3.1. Methods to calculate the fraction of light absorbed by chlorophyll in broadleaf and needleleaf plants

We have used the following equation to calculate the fraction of light absorption by chlorophyll in the canopy ($FPAR_{chl}$): $FPAR_{chl} = a * EVI - b$. In the VPM v1.0 (Xiao et al. 2004), and VPM v2.0 (Zhang et al. 2017), we treat both flat (broad) leaf and needleleaf with the same equation. In the VPM 3.0, we treat broadleaf and needleleaf with different parameter values.

$$\text{Broadleaf}: \ FPAR_{chl-broadleaf} = EVI - 0.1 \quad (6)$$

$$\text{Needleleaf}: \ FPAR_{chl-needleleaf} = 1.25*EVI - 0.1 \quad (7)$$

We assume $a = 1.25$ in Eq. (7) after we carried out both literature review of empirical studies and leaf-trait-based calculation. Among the literature review of empirical studies, one study at the MS-Me2 site (Law et al. 2001) reported needle-to-shoot area ratio of 1.25 and used it to adjust leaf area index estimates of needleleaf trees at the site. Here we briefly explain our assumption from the perspective of needleleaf structure or leaf trait. At the leaf level, in the cross-section of a needleleaf, the distribution of chloroplasts is arranged in circle and can be approximated as a ring (Fig. 5d). The inner part of the needleleaf are transport tissue and endoderm, and the outer part is wrapped by mesophyll, and chloroplasts are distributed in mesophyll (Trueba et al. 2022). The ratio of mesophyll volume to total leaf volume is assumed as the ratio of ring area to the concentric circle area, and one study reported the ratio (γ_E) as 1.27 (1.28) based on mean (medium) values of 34 species across conifer plants (Trueba et al. 2022). Here we use a simple way to estimate the ratio ($g_{needleleaf}$) (Fig. 5, Eq. (8)). At the cross-section, leaf area from a flat-shape broadleaf (e.g., width = 5 mm) is smaller than leaf area from a needleleaf (e.g., diameter = 5 mm), as needleleaf has a cylindrical shape and its perimeter is larger than diameter (Fig. 5b, d). The ratio of the perimeter from the outer semi-circle over the diameter is pi/2 (3.14/2 = 1.57). We simply assume $\frac{R_3}{R_1}$ as 0.8 and then γ_E was about 1.2566, ~1.26. In this study, for simplicity and imperfect circle of a needleleaf, we used 1.25 for needleleaf at the three sites. Here we assume that these two approaches (our leaf structure approach vs the needle-to-shoot area approach) offer similar solutions to adjust the light absorption of ENF.

$$\gamma_E = \frac{\frac{1}{2} \times 2 \times \pi \times R_3}{2 \times R_1} = \frac{\pi}{2} \times \frac{R_3}{R_1} \quad (8)$$

To fully consider the light absorbed by needle leaves at three ENF sites, we multiplied the needle-to-flat area ratio (γ_E, 1.25) to calculate $FPAR_{chl\text{-}needleleaf}$ and we considered that green vegetation didn't exist when EVI is <0.1, at which $FPAR_{chl\text{-}needleleaf}$ is 0:

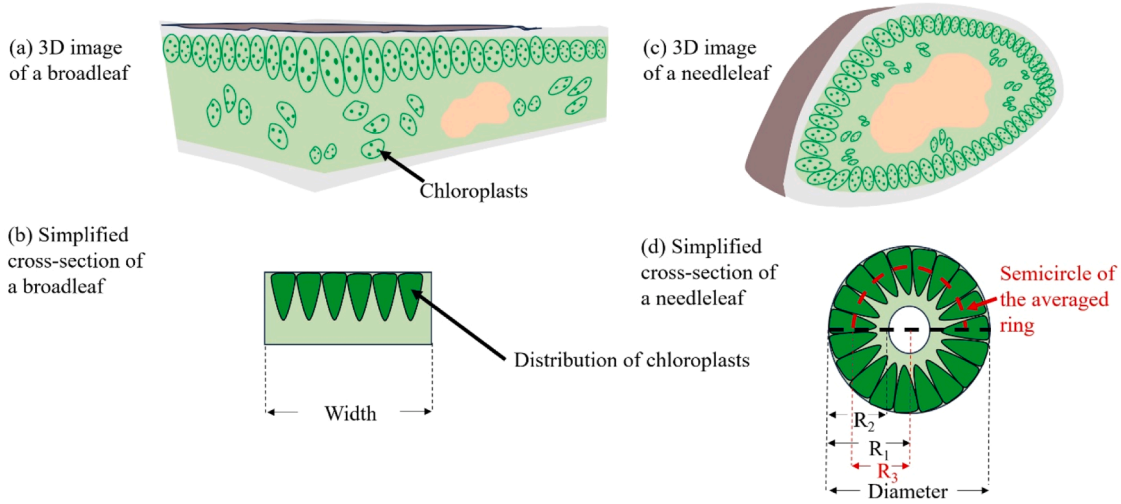

Fig. 5. Three-dimensional (3D, cross-session) diagrams of (a) broadleaf and (c) needleleaf. Solid green dots represent chloroplasts. Simplified cross-section of (b) broadleaf and (d) needleleaf; the green triangles represent the distribution of chloroplasts. In (d), R_1 represents the radius of the concentric circle, R_2 represents the width of the ring and R_3 represents the width of the averaged ring.

$$FPAR_{chl-needleleaf} = \begin{cases} 0, & EVI \le 0.1 \\ 1.25 \times EVI - 0.1, & EVI > 0.1 \end{cases} \quad (9)$$

2.3.2. Methods to estimate site-specific apparent optimum air temperature for photosynthesis of evergreen needleleaf forests ($T_{opt\text{-}site}$)

T_{scalar} ranges from 0 to 1 and is calculated as follows:

$$T_{scalar} = \frac{(T - T_{max}) \times (T - T_{min})}{(T - T_{max}) \times (T - T_{min}) - (T - T_{opt})^2} \quad (10)$$

where the T, T_{max}, T_{min} and T_{opt} refer to the daytime mean air temperature, and maximum, minimum, and optimum air temperature parameters for photosynthesis, respectively. T_{min} and T_{max} can be obtained from a look-up table (Zhang et al. 2017).

In both VPM v1.0 and v2.0, we used biome-specific T_{opt} ($T_{opt\text{-}biome}$) parameter values. Our previous studies reported the procedure to estimate site-specific T_{opt} ($T_{opt\text{-}site}$) parameter values by (1) GPP_{EC} versus air temperature response curves and (2) EVI versus air temperature response curves, where air temperature data are from the in-situ measurements at the tower sites or the climate data products (Chang et al. 2021; Chang et al. 2020). In specific, the site-year specific T_{opt} ($T_{opt\text{-}site\text{-}year}$) is determined by averaging the temperature (T_{DT}) corresponding to the 95th percentile of peak GPP_{EC} (or EVI) values in the response curves for that year. Then, $T_{opt\text{-}site}$ is obtained by averaging $T_{opt\text{-}site\text{-}year}$ values across multiple years, excluding those years in which the number of air temperature observations accounted for <50 % of the total possible observations during the snow-free season. For the US-Ho2 and US-NR1 sites, the observations during the snow-free seasons were used. For the US-Me2 site, the observations from mid-May to late-July are used. We estimated $T_{opt\text{-}site\ (GPPec\ -\ Tec)}$ and $T_{opt\text{-}site\ (EVI\ -\ Tec)}$ by using the air temperature data from the tower sites, and $T_{opt\text{-}site\ (GPPec\ -\ Tera5)}$ and $T_{opt\text{-}site\ (EVI\ -\ Tera5)}$ by using the air temperature data from the ERA5 data products (Table 3).

2.3.3. Methods to estimate effect of water on GPP

W_{scalar} ranges from 0 to 1 and is calculated as follows:

$$W_{scalar} = \frac{1 + LSWI}{1 + LSWI_{max}} \quad (11)$$

$LSWI_{max}$ is the maximum LSWI during the snow-free season in a year. To reduce any bias, a temporal smoothing technique is employed, encompassing data from the four adjacent years (two years preceding and two years following), to determine the second highest $LSWI_{max}$ over this five-year timeframe, which will be used as input "$LSWI_{max}$" (Zhang et al. 2017). W_{scalar} represents the water stress from land surface (including both plant leaves and soils).

The Mediterranean climate is characterized with a wet season and a dry season, thus evergreen forests under this climate condition often develop deep roots for access to deep soil water. The forest at the US-Me2 site have deep roots to get water from the ground during the dry seasons (Thomas et al. 2009). The deep roots also have access to water throughout the soil profiles in the wet season, too, which may further ensure plants free from water stress during the wet season. Thus, for the US-Me2 site, we set $W_{scalar} = 1$ at the US-Me2 site during the wet seasons

Table 3
ε_0 and air temperature parameter values used in the VPM for the three sites. Minimum and maximum air temperature parameters were from the leaf-based laboratory experiment. Biome-optimal air temperature parameters were defined in biome-specific lookup tables. Site-specific air temperature ($T_{opt\text{-}site}$) were calculated by the methods in Section 2.3.2.

Site_ID Parameter	US-Ho2	US-NR1	US-Me2
ε_0 (g C/mol APAR)	0.53	0.53	0.53
T_{min} (°C)	−1	−1	−1
T_{max} (°C)	40	40	40
$T_{opt\text{-}biome}$ (°C)	20	20	20
$T_{opt\text{-}site\text{-}(GPPec\ -\ Tec)}$ (°C)	22	14	16
$T_{opt\text{-}site\text{-}(EVI\ -\ Tec)}$ (°C)	20	13	16
$T_{opt\text{-}site\text{-}(GPPec\ -\ Tera5)}$ (°C)	23	17	19
$T_{opt\text{-}site\text{-}(EVI\ -\ Tera5)}$ (°C)	22	16	19

(January to June, October to December), and calculated W_{scalar} as Eq. (11) during the dry season (July to September).

2.4. Simulations of VPM v3.0 under two $FPAR_{chl}$ estimates, climate datasets and two w_{scalar} parameters

We run and compare the VPM simulations (Table S1): (1) two $FPAR_{chl}$ estimates (with or without 1.25 in $FPAR_{chl}$ estimation), (2) two meteorological datasets (EC vs ERA5), (3) two $T_{opt\text{-}site}$ estimates with ERA5 climate data ($T_{opt\text{-}site\text{-}GPP}$ vs $T_{opt\text{-}site\text{-}EVI}$). For additional information on the VPM simulations, please consult Supplementary Methods #1.

2.5. Statistical analyses

2.5.1. GPP_{EC}, vegetation indices, and air temperature comparison

To investigate the relationships between GPP_{EC} and vegetation indices (NDVI and EVI), the relationships between GPP_{EC} and $T_{DT\text{-}EC}$, and the relationships between EVI and $T_{DT\text{-}EC,}$ we employed simple linear regression analysis. This analysis was based on two statistical measures for comparison: slope (α) and the coefficient of determination (R^2) (Janssen and Heuberger 1995). Details on the calculation of the slope (α) and intercept (b) in the linear regression equation ($y = \alpha * x + b$) can be found in Supplementary Methods #2.

2.5.2. Comparison between predicted GPP (GPP_{VPM}) and estimated GPP (GPP_{EC})

To quantify the difference or agreement of GPP datasets from two methods, for example, predicted GPP by models (GPP_{VPM}; y) versus estimated GPP (GPP_{EC}; x) by partitioning of NEE data at the tower site, we used a simple linear regression ($GPP_{VPM} = \alpha * GPP_{EC}$; $y = \alpha * x$, no intercept) with three statistical measures: slope (α), R^2 and RMSE. In this study, the slope (α) was calculated with the y-intercept set to zero ($GPP_{VPM} = \alpha * GPP_{EC}$), following the approach described in Supplementary Methods #3 (Pan et al. 2024a). We used $y = \alpha * x$ to assess whether GPP_{VPM} overestimates ($\alpha > 1$) or underestimates ($\alpha < 1$) GPP_{EC}. This $y = \alpha * x$ approach has been used in previous studies for comparison between predicted GPP and estimated GPP_{EC} (Chang et al. 2021; Pan et al. 2024a; Zhang et al. 2017). See Supplementary Methods 2 and Methods 3 for more information on the simple linear regression models in the equation of $y = \alpha * x + b$ and in the equation of $y = \alpha * x$.

3. Results

3.1. Seasonal dynamics of climate, vegetation indices and carbon fluxes

At the US-Ho2 site, PAR_{EC} (Fig. 6a) has a strong seasonal dynamic, ranging from ~10 mol/day in winter to ~45 mol/day in summer. $T_{DT\text{-}EC}$ also had a strong seasonal dynamic with a winter season from late-November to February (<= 0 °C), and rose to ~5 °C in April, and reached its peak (~22 °C) in August. The seasonal dynamics of P_{EC} had moderate precipitation in spring, small precipitation in July, and large precipitation in late fall and winter (snowy winter). High LSWI values in the winter season (late-November to February) indicate snow cover in the site (Fig. 6b), and LSWI shows that snow-free season starts in April and ends in November. After the snow melt in spring, NDVI, EVI, and LSWI began to increase by mid-March (Fig. 6b), stabilized at a high level during the summer, and then declined gradually. GPP_{EC} (Fig. 6c) experienced a swift rise in April (1 g C/m^2/day or higher), peaked in July, and fell to below 1 g C/m^2/day by mid-November.

At the US-NR1 site, PAR_{EC} (Fig. 6d) exhibited strong seasonal dynamics, ranging from ~15 mol/day in the winter to ~50 mol/day in June. $T_{DT\text{-}EC}$ displayed a seasonal pattern with a winter season from early-November to mid-April (<= 0 °C) and rose to approximately 5 °C in mid-May, and reached a peak of around 15 °C in mid-July. P_{EC} had a moderate seasonal dynamic, relatively small amount of precipitation in the winter season (mostly snow), and large amount of precipitation in the summer. SWC_{EC} stabilized at ~8 % from December to early April, rose rapidly in mid-April, peaked at ~30 % in early June, then declined steadily until early August, and has been around 10 % since then. High LSWI in the winter season (late-October to April) indicates snow cover at the site (Fig. 6e) and LSWI shows that snow-free season starts in late April and ends in October. As snow melts in spring (March-May) and June, NDVI and EVI rose in May and peaked in late-July (~0.75 for NDVI) and in early-July (~0.4 for EVI). GPP_{EC} (Fig. 6f) rose in late-April (1 g C/m^2/day or higher), peaked in mid-July, and fell to below 1 g C/m^2/day by late-October.

At the US-Me2 site, PAR_{EC} (Fig. 6 g) exhibited a distinct seasonal dynamic, with values ranging from ~10 mol/day in winter to ~60 mol/day in July. $T_{DT\text{-}EC}$ showed a marked seasonality with the winter season from December to early-January (<= 0 °C), and then rose to 5 °C in mid-April and peaked at ~22 °C in early-August. The seasonal dynamics of P_{EC} were characterized by little to small amounts of precipitation in summer (July-September), and moderate to large amounts of precipitation in the other seasons (Fig. 6 g). From January to April, the SWC_{EC} stayed above 30 %. It began to decline continuously from mid-April until it reached 10 % by late July. It then held steady at 10 % from July to September, before rising sharply in early October, and nearing 30 % again by the end of December. High LSWI in the winter season indicated snow cover (Fig. 6h) and LSWI showed that snow-free season starts from March and ends in November. NDVI and EVI increased gradually from early-April to mid-November (Fig. 6h), with both curves reaching a peak in mid-November. GPP_{EC} (Fig. 6i) was low in the winter season and rose rapidly in March and reached peak by early-July. The large drop in GPP_{EC} over the period of mid-July to September reflects the effect of limited water availability on GPP during the dry and hot July - September.

We delineated the snow-free seasons by $T_{DT\text{-}EC}$ consistently higher than 5 °C at three sites (Fig. 7). For US-Ho2 site (Fig. 7a), the calculated snow-free seasons ranged from late-April to early-November. The absence of an end date for the snow-free season in 2014 and the unusually short snow-free season in 2015 were due to a lack of $T_{DT\text{-}EC}$ data from early October 2014 to early September 2015. For the US-NR1 site (Fig. 7b), the calculated snow-free seasons ranged from June to October. For the US-Me2 site (Fig. 7c), the calculated snow-free seasons ranged from early-February to late November with large difference varied years. The 2006 result was shorter than the remaining years because of missing $T_{DT\text{-}EC}$ data from January through mid-June 2006. The absence of an end date for 2011 was attributed to a lack of $T_{DT\text{-}EC}$ data from mid-November to mid-December 2011.

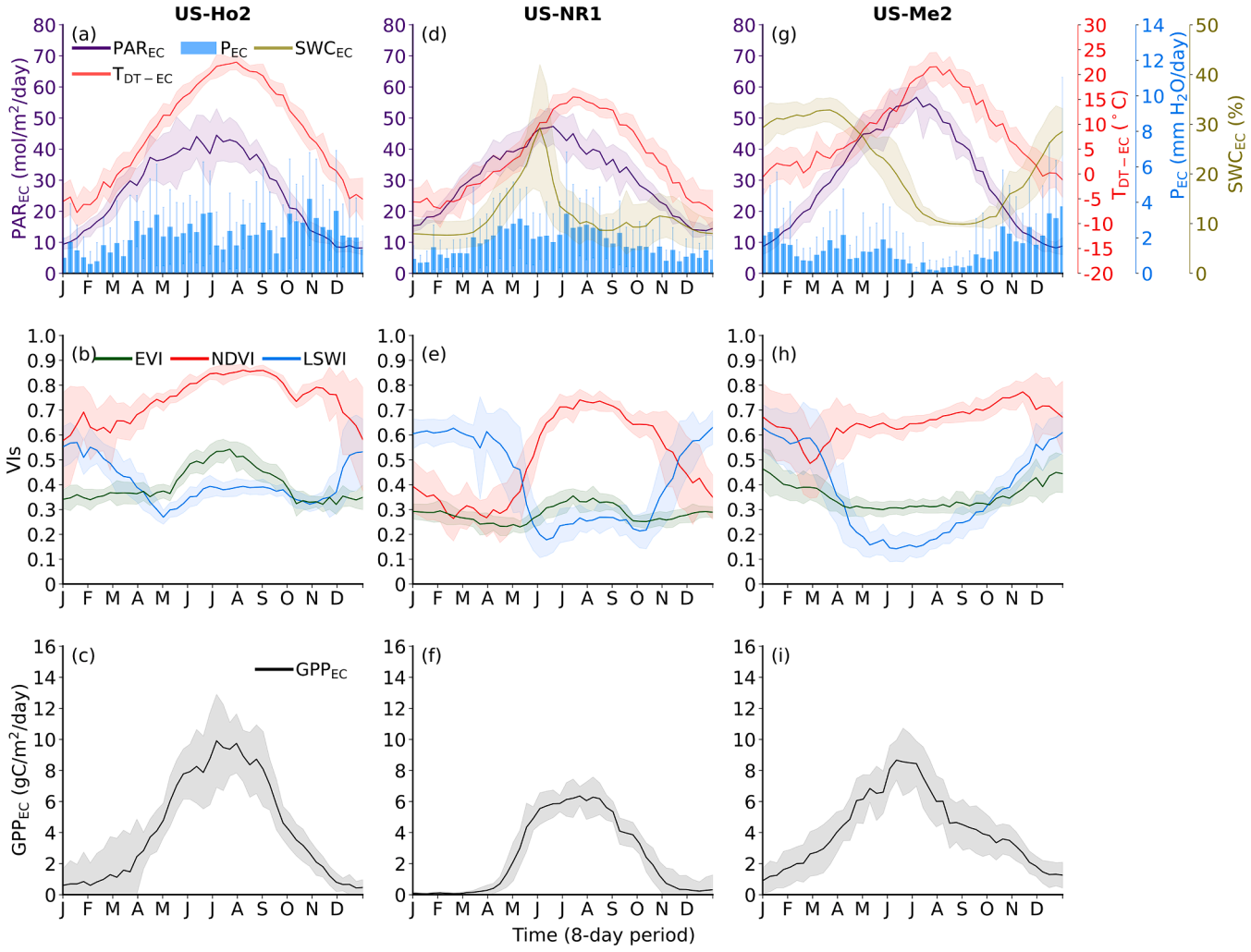

Fig. 6. Multi-year averaged seasonal dynamics of photosynthetically active radiation (PAR_{EC}), air temperature ($T_{DT\text{-}EC}$), precipitation (P_{EC}), soil water content (SWC_{EC}), vegetation indices (NDVI, EVI, LSWI), and carbon fluxes (GPP_{EC}) at three evergreen needleleaf forest sites: (a~c) US-Ho2, from 2007 to 2020; (d~f) US-NR1, from 2000 to 2016; (g~i) US-Me2, from 2002 to 2019. Solid lines and light blue bars represent multi-year averages. The shadows indicate the range (standard deviation) of variables over multiple years.

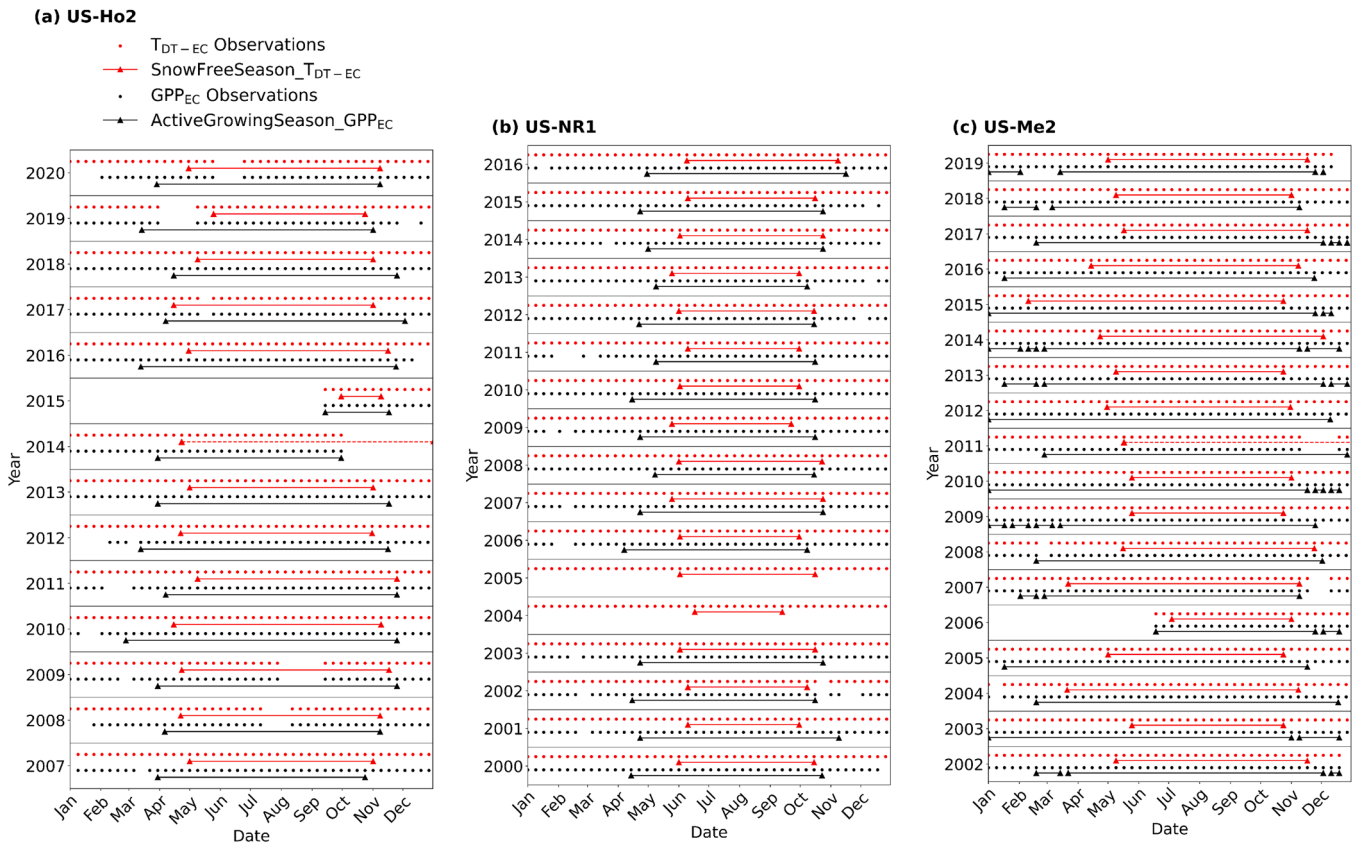

Fig. 7. The snow-free season delineated by T_{DT-EC}, and active growing season delineated by both T_{DT-EC} and GPP_{EC}. (a) US-Ho2, 2007–2020; (b) US-NR1, 2000–2016; (c) US-Me2, 2002–2019.

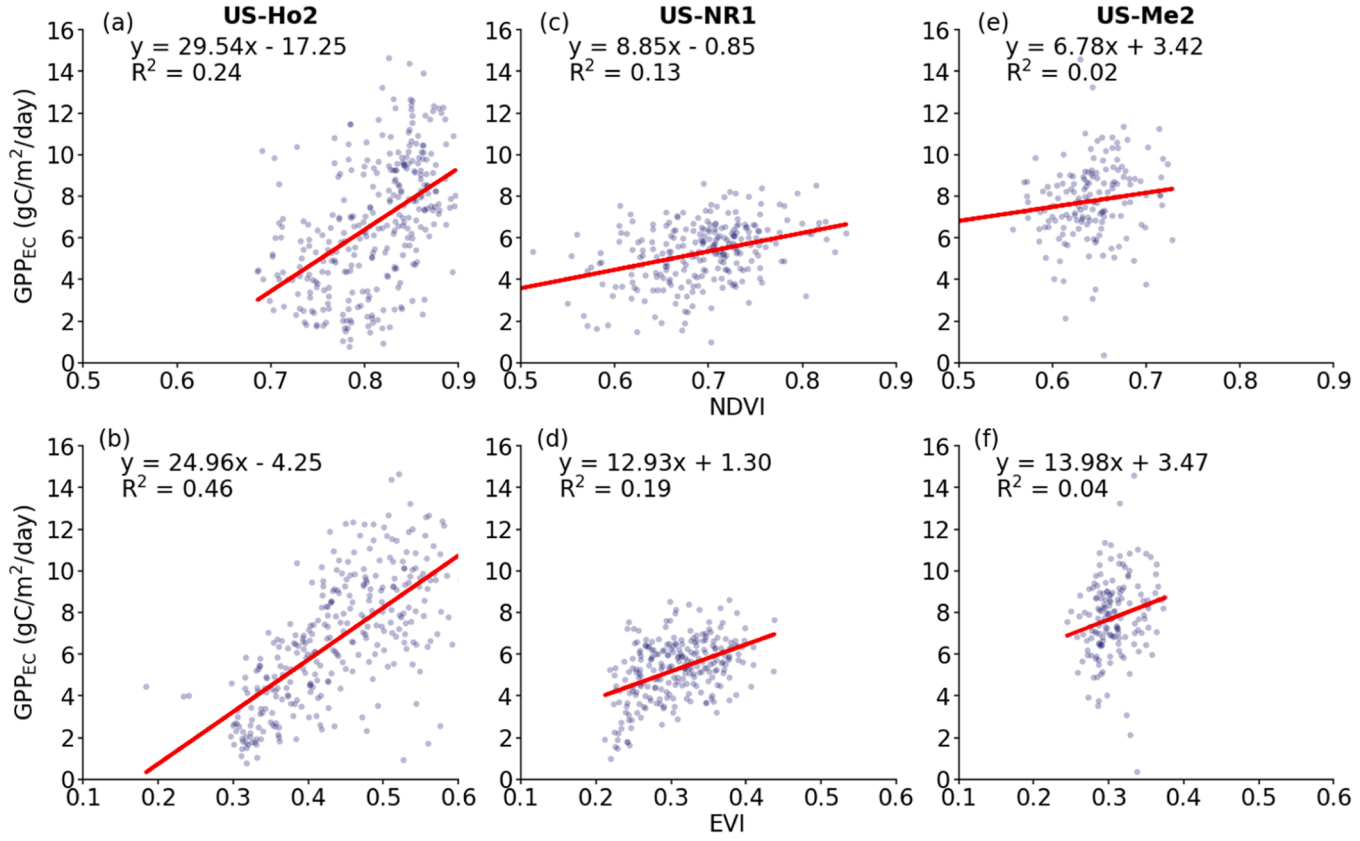

Fig. 8. Relationships between GPP_{EC} and vegetation indices (NDVI, EVI) at three evergreen needleleaf forest sites during snow-free seasons. (a~b) US-Ho2, snow-free seasons (2007–2020); (c~d) US-NR1, snow-free seasons (2000–2016); (e~f) US-Me2, mid-May to late-July (2002–2019). The darker the color of the scatterplot, the more dots there are.

We delineated the active growing seasons by $T_{DT\text{-}EC}$ higher than −1 °C and GPP_{EC} higher than 1 g C/m^2/day at three sites (Fig. 7). For the US-Ho2 site (Fig. 7a), the calculated active growing seasons ranged from March to November. Short results for 2014 and 2015 were attributed to a lack of GPP_{EC} data from early October 2014 to early September 2015. For US-NR1 site (Fig. 7b), the calculated active growing seasons ranged from mid-April to mid-November. Missing results for 2004 and 2005 were attributed to a lack of GPP_{EC} data from 2004 to 2005. For the US-Me2 site (Fig. 7c), active growth could occur at any time of the year. The 2006 result was shorter than the remaining years because of missing GPP_{EC} data from January through mid-June 2006.

3.2. Quantitative relationships between GPP_{EC}, vegetation indices, and air temperature

The relationships between GPP_{EC} and vegetation indices (NDVI and EVI) were plotted for the three sites (Fig. 8). At the US-Ho2 and US-NR1 sites, the relationship between GPP_{EC} and VIs (NDVI and EVI) during the snow-free seasons was positive (Fig. 8a∼d). At the US-Me2 site (Fig. 8e∼f), we analyzed relationships between GPP_{EC} and vegetation indices from mid-May to late-July, a period when GPP_{EC} reaches its peak. This approach was chosen instead of considering the entire snow-free seasons, as the seasonal dynamics of GPP_{EC} do not closely correspond to those of vegetation indices throughout the entire growing season at the US-Me2 site (Fig. 6h∼i). At the three sites, GPP_{EC} had stronger relationships (higher R^2) with EVI than NDVI.

We analyzed the relationships between GPP_{EC} and $T_{DT\text{-}EC}$ at three sites. At the US-Ho2 site (Fig. 9a), GPP_{EC} rose with increasing temperature, peaked at 21 °C, and then decreased slightly after 23 °C. At the US-NR1 site (Fig. 9c), GPP_{EC} rose with temperature, peaked at ∼14 °C, and then decreased after ∼16 °C. At the US-Me2 site (Fig. 9e), GPP_{EC} increased with temperature up to a stable point at ∼14 °C, and then decreased after ∼17 °C. As described in Section 2.3.2, $T_{opt\text{-}site\ (GPP\text{-}Tec)}$ estimates at the three sites are approximately 22 °C (US-Ho2), 14 °C (US-NR1) and 16 °C (US-Me2), respectively.

We explored the relationships between EVI and $T_{DT\text{-}EC}$ at the three sites. At the US-Ho2 site (Fig. 9b), EVI rose with temperature to a maximum at ∼21 °C, and then decreased slightly when temperature kept increasing. At the US-NR1 site (Fig. 9d), EVI increased with warming up to a peak at approximately 15 °C, and then decreased after 17 °C. At the US-Me2 site (Fig. 9f), EVI increased slightly to reach a plateau at approximately 16 °C. Finally, EVI turned to decrease after 18 °C. As described in the Section 2.3.2, $T_{opt\text{-}site\ (EVI\text{-}Tec)}$ estimates at the three sites are 20 °C (US-Ho2), 13 °C (US-NR1) and 16 °C (US-Me2), respectively.

This study first showed that EVI has a stronger relationship with GPP_{EC} than does NDVI, supporting the choice of EVI for subsequent analyses. We then examined the relationship between GPP_{EC} and air temperature to determine site-specific apparent optimal temperatures ($T_{opt\text{-}site\ (GPP\text{-}Tec)}$). We analyzed the relationship between EVI and air temperature with an aim to derive site-specific apparent optimal temperatures from analyses of EVI ($T_{opt\text{-}site\ (EVI\text{-}Tec)}$) and air temperature data. As the numbers of eddy flux tower sites with GPP_{EC} data are limited, this EVI-based approach provides a pathway for estimating $T_{opt\text{-}site}$ over the land surface in the globe by using EVI data, which can be derived from surface reflectance data, and air temperature dataset such as ERA5. Our recent publication released the global $T_{opt\text{-}site}$ dataset from analyses of MODIS and ERA5 data (Pan et al. 2024b).

3.3. Comparison between GPP_{EC} and GPP_{VPM} from simulation of VPM v3.0 with in-situ climate data

At the US-Ho2 site, we compared GPP_{EC} and GPP_{VPM} from two simulations of VPM v3.0: (1) $FPAR_{chl}$ = EVI - 0.1, EC site climate data,

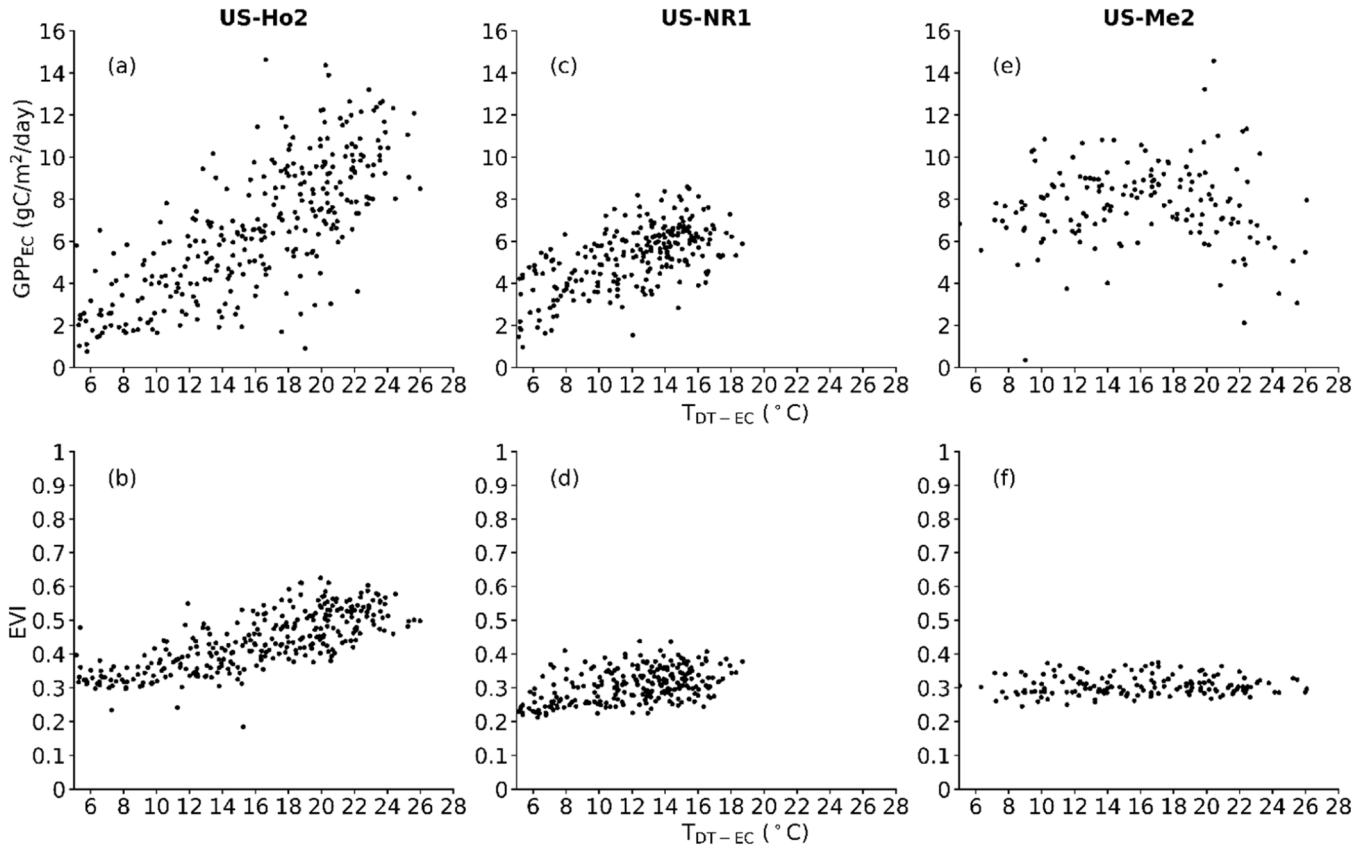

Fig. 9. The relationships between GPP_{EC} and $T_{DT\text{-}EC}$, and relationships between EVI and $T_{DT\text{-}EC}$ at three evergreen needleleaf forest sites. (a∼b) US-Ho2, snow-free seasons (2007–2020); (c∼d) US-NR1, snow-free seasons (2000–2016); (e∼f) US-Me2, mid-May to late-July (2002–2019).

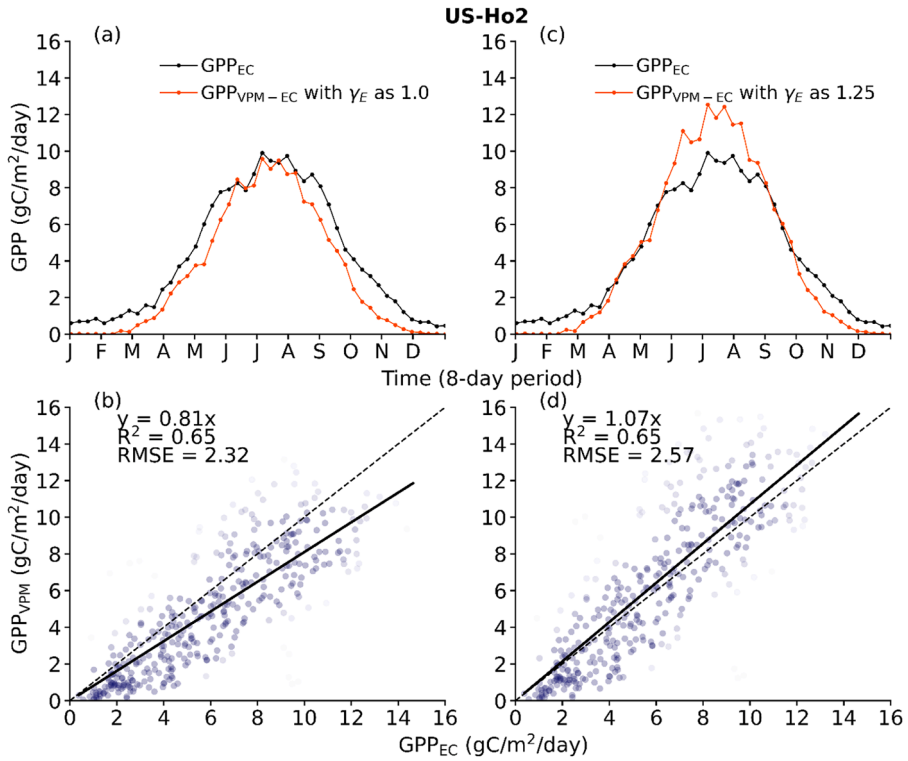

Fig. 10. (US-Ho2 site) Seasonal dynamics of $GPP_{VPM\text{-}EC}$, $GPP_{VPM\text{-}ERA5}$ and GPP_{EC} at US-Ho2 site, which are averaged from 2007 to 2020. The comparison between GPP_{VPM} and GPP_{EC} at US-Ho2 site during active growing seasons from 2007 to 2020. (a~b) $GPP_{VPM\text{-}EC}$ with γ_E as 1.0; (c~d) $GPP_{VPM\text{-}EC}$ with γ_E as 1.25. The active growing seasons are defined by $T_{DT\text{-}EC}$ and GPP_{EC}. The darker the color of the scatterplot, the more dots there are.

and (2) $FPAR_{chl} = 1.25 * EVI - 0.1$, EC site climate data (Fig. 10). The use of new needleleaf-specific $FPAR_{chl}$ equation substantially improves the seasonal dynamics of GPP_{VPM} in comparison to that of GPP_{EC}. In specific, although the RMSE for US-Ho2 increased slightly from 2.32 to 2.57 (Fig. 10b vs. Fig. 10d), the slope improved significantly from 0.81 to 1.07, indicating a shift from substantial underestimation (−19 %) to moderate overestimation (+7 %). Both RMSE and slope are important metrics for evaluating model performance, and the improved slope indicates better agreement with GPP_{EC} trends.

At the US-NR1 site, we conducted the same analysis as at the US-Ho2 site, using the two simulations of VPM v3.0 described above (Fig. 11). The use of new needleleaf-specific $FPAR_{chl}$ equation substantially improves the seasonal dynamics of GPP_{VPM} in comparison to that of GPP_{EC}.

At the US-Me2 site, we compared GPP_{EC} and GPP_{VPM} from three simulations of VPM v3.0: (1) $FPAR_{chl} = EVI - 0.1$, W_{scalar} as calculated, EC site climate data, (2) $FPAR_{chl} = 1.25 * EVI - 0.1$, W_{scalar} as calculated, EC site climate data, and (3) $FPAR_{chl} = 1.25 * EVI - 0.1$, W_{scalar} as 1.0 during wet seasons while W_{scalar} as calculated during dry seasons, EC site climate data (Fig. 12). The use of new needleleaf-specific $FPAR_{chl}$ equation substantially improves the seasonal dynamics of GPP_{VPM} in comparison to that of GPP_{EC} (Fig. 12a,b vs. Fig. 12c,d). The use of W_{scalar} as 1.0 during wet seasons also substantially improves the seasonal dynamics of GPP_{VPM} in comparison to that of GPP_{EC} (Fig. 12c,d vs. Fig. 12e, f). This is due to the high soil water content during the wet seasons and the plants' deep roots, which allow them to access water and grow without being limited by water availability.

3.4. Comparison between GPP_{EC} and GPP_{VPM} from simulation of VPM v3.0 with ERA5 climate data

In Section 3.3, we ran different VPM simulations with site-specific climate data and identified the best model-setup based on two criteria: (1) how well the multi-year averaged GPP_{VPM} time series captured the seasonal dynamics of GPP_{EC}, and (2) how well the GPP_{VPM} aligned with GPP_{EC} data during the active growing season over years, by using 2-D scatter plots and a simple statistical model ($GPP_{VPM} = a * GPP_{EC}$; slope, R^2, and RMSE). In this section, we selected the best simulation setup and ran simulations of VPM v3.0 with ERA5 climate data and then we compared the resultant $GPP_{VPM\text{-}ERA5}$ with GPP_{EC} data.

For the US-Ho2 site, we compared GPP_{EC} with $GPP_{VPM\text{-}ERA5}$ simulated using $FPAR_{chl} = 1.25 * EVI - 0.1$ and ERA5 climate data (Fig. 13a~b). The simulated $GPP_{VPM\text{-}ERA5}$ captured the seasonal dynamics of GPP_{EC} well, as shown by the close match in the multi-year average time series (Fig. 13a). Additionally, when comparing individual observations across multiple years, the results showed a strong correlation, with an R^2 of 0.64 and slope of 1.08 (Fig. 13b). The results were very similar to those from the previous comparison of GPP_{EC} with $GPP_{VPM\text{-}EC}$ simulated using the same model ($FPARchl = 1.25 * EVI - 0.1$) but driven by EC site climate data (Fig. 10c~d). This is primarily due to minor differences between the EC site climate data and ERA5 climate data at this site (Fig. 4a~b).

For the US-NR1 site, we compared GPP_{EC} with $GPP_{VPM\text{-}ERA5}$ simulated using $FPAR_{chl} = 1.25 * EVI - 0.1$ and ERA5 climate data (Fig. 13c~d). The results showed notable differences compared to the previous comparison of GPP_{EC} with $GPP_{VPM\text{-}EC}$ simulated using the same model but driven by EC site climate data (Fig. 11c~d). These differences are primarily driven by significant discrepancies between the EC site climate data and ERA5 climate data at the US-NR1 site (Fig. 4c~d).

For the US-Me2 site, we compared GPP_{EC} with $GPP_{VPM\text{-}ERA5}$ simulated using the following model settings: (1) $FPAR_{chl} = 1.25 * EVI - 0.1$, and (2) W_{scalar} as 1.0 during wet seasons while W_{scalar} as calculated during dry seasons (July to September). The $GPP_{VPM\text{-}ERA5}$ was simulated by ERA5 climate data (Fig. 13e~f). The results showed moderate differences compared to the previous comparison of GPP_{EC} with $GPP_{VPM\text{-}EC}$ simulated using the same model settings but driven by EC site climate data (Fig. 12e~f). These differences are driven by moderate differences between EC site climate data and ERA5 climate data at the US-Me2 site (Fig. 4e~f).

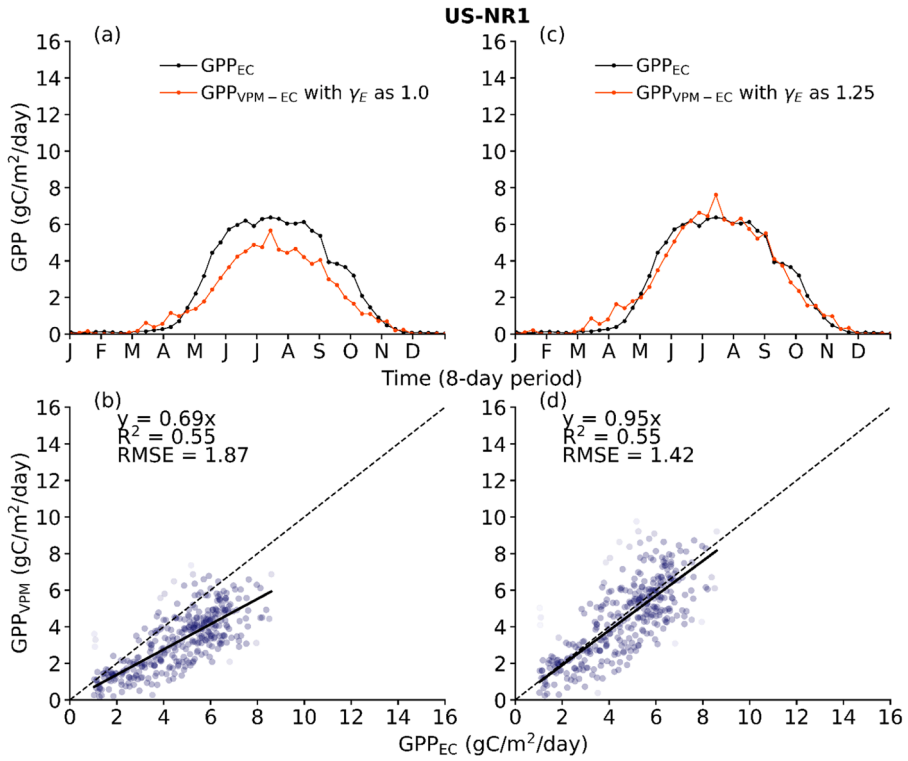

Fig. 11. (US-NR1 site) Seasonal dynamics of $GPP_{VPM\text{-}EC}$, $GPP_{VPM\text{-}ERA5}$ and GPP_{EC} at US-NR1 site, which are averaged from 2000 to 2016. The comparison between GPP_{VPM} and GPP_{EC} at US-NR1 site during active growing seasons from 2000 to 2016. (a~b) $GPP_{VPM\text{-}EC}$ with γ_E as 1.0; (c~d) $GPP_{VPM\text{-}EC}$ with γ_E as 1.25. The active growing seasons are defined by $T_{DT\text{-}EC}$ and GPP_{EC}. The darker the color of the scatterplot, the more dots there are.

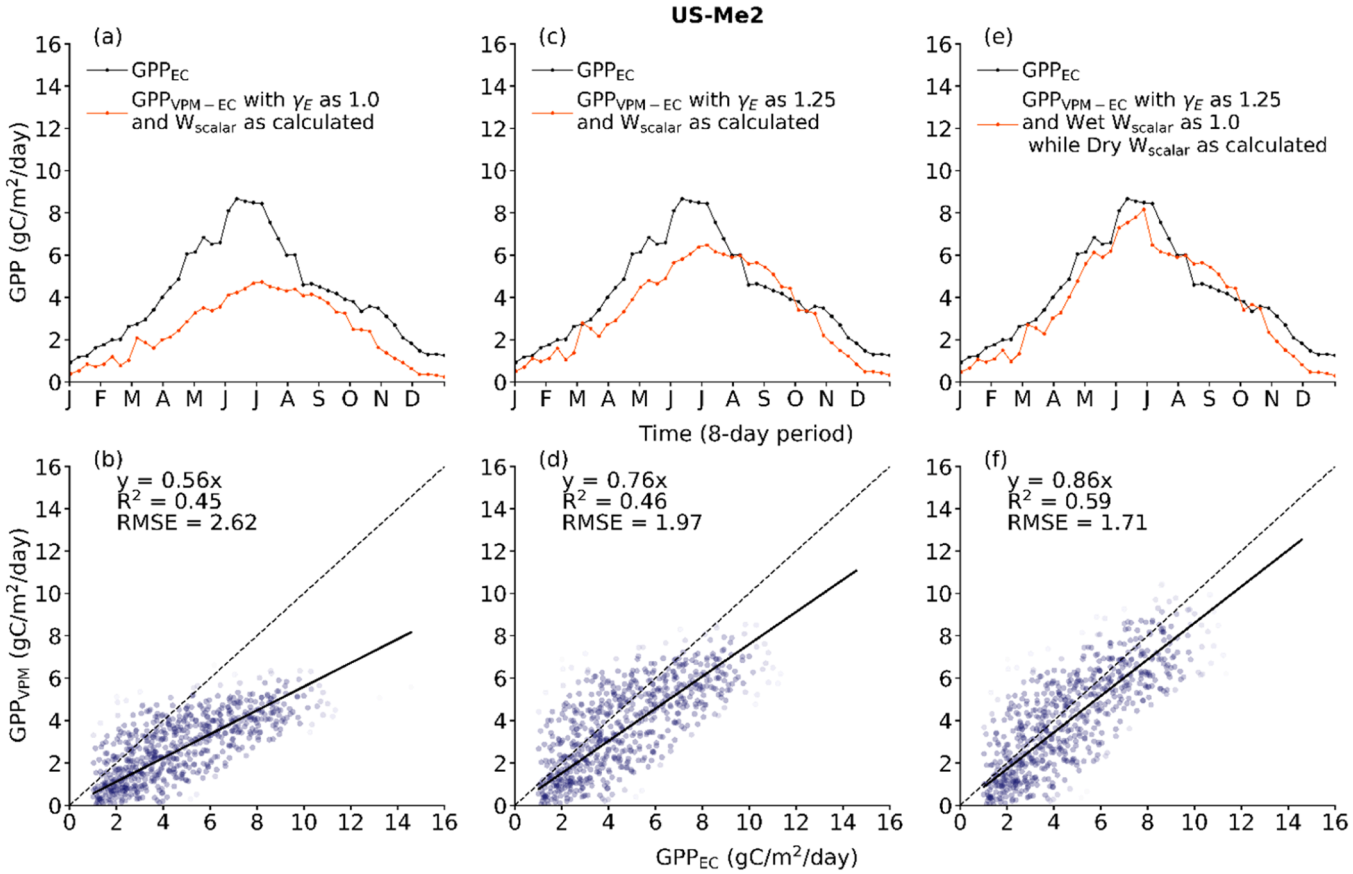

Fig. 12. (US-Me2 site) Seasonal dynamics of $GPP_{VPM\text{-}EC}$, $GPP_{VPM\text{-}ERA5}$ and GPP_{EC} at US-Me2 site, which are averaged from 2002 to 2019. The comparison between GPP_{VPM} and GPP_{EC} at US-Me2 site during active growing seasons from 2002 to 2019. (a~b) $GPP_{VPM\text{-}EC}$ with γ_E as 1.0 and W_{scalar} as calculated; (c~d) $GPP_{VPM\text{-}EC}$ with γ_E as 1.25 and W_{scalar} as calculated; (e~f) $GPP_{VPM\text{-}EC}$ with γ_E as 1.25 and W_{scalar} as 1.0 during wet seasons while W_{scalar} as calculated during dry seasons. The active growing seasons are defined by $T_{DT\text{-}EC}$ and GPP_{EC}. The darker the color of the scatterplot, the more dots there are.

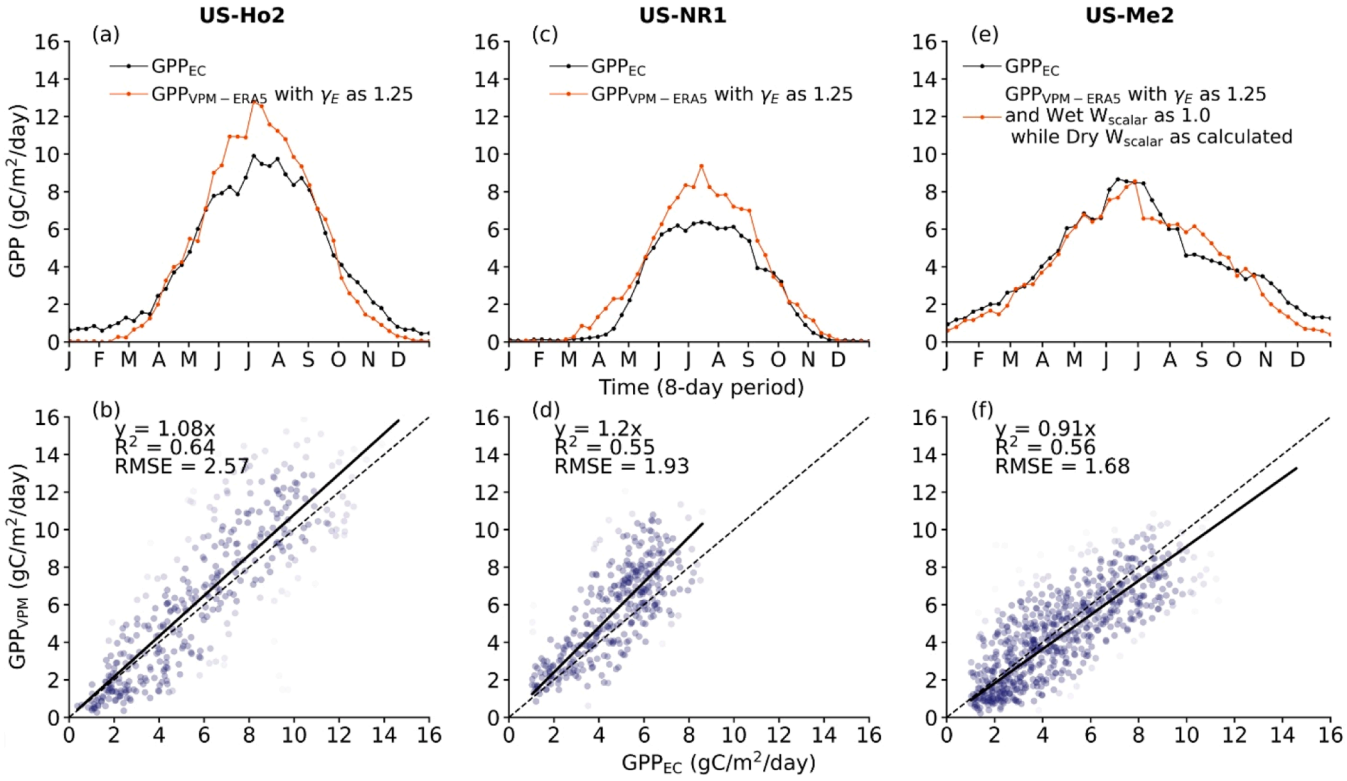

Fig. 13. Seasonal dynamics of $GPP_{VPM\text{-}ERA5}$ and GPP_{EC} at three sites: (a~b) US-Ho2 (2007–2020), $GPP_{VPM\text{-}ERA5}$ with γ_E as 1.25 and W_{scalar} as calculated; (c~d) US-NR1 (2000–2016), $GPP_{VPM\text{-}ERA5}$ with γ_E as 1.25 and W_{scalar} as calculated; (e~f) US-Me2 (2002–2019), $GPP_{VPM\text{-}ERA5}$ with γ_E as 1.25 and W_{scalar} as 1.0 during wet seasons while W_{scalar} as calculated during dry seasons. The comparison between $GPP_{VPM\text{-}ERA5}$ and GPP_{EC} during active growing seasons of each year. The active growing seasons are defined by $T_{DT\text{-}EC}$ and GPP_{EC}. The darker the color of the scatterplot, the more dots there are.

Overall, the results show that substituting ERA5 climate data for EC measurements results in limited differences at the studied sites, which are characterized by different climate and soil water conditions. ERA5 climate data are used as it offers global coverage, making it an essential dataset for simulations of VPM v3.0 over those areas without local climate data.

4. Discussion

4.1. Biophysical performance of vegetation indices in evergreen needleleaf forests under three different climate types

Vegetation indices have been widely used to investigate vegetation canopy dynamics (Huete et al. 2002). One study reported temporal consistency between monthly vegetation indices (NDVI and EVI) and air temperature among 12 ENF sites over the central North America (Liu et al. 2016). Evergreen needleleaf forests are characterized with green leaves throughout the year and these green leaves have different ages (from months to one year and multiple years old leaves), therefore, the seasonal dynamics of vegetation indices reflects the combined effects of both leaf area index and the mixed ratio of young, mid-age, and old leaves in the ENF canopies. At the US-Ho2 and US-NR1 sites, the seasonal dynamics of PAR_{EC}, $T_{DT\text{-}EC}$ and precipitation were synchronous over the season (Fig. 6a, d). The presence of snow cover during winter leads to higher values in the RED band, resulting in low NDVI. As the snowpack melts after winter season, surface reflectance values in RED band decrease and NDVI values increase. Trees grow new leaves in later spring and early summer, which contributes only moderately to the rise of NDVI and EVI in that period. In comparison, at the US-Me2 site, the seasonal dynamics of PAR_{EC}, $T_{DT\text{-}EC}$ and precipitation were asynchronous over the season (Fig. 6 g), which represents typical Mediterranean climate that is characterized by hot and dry summer, and warm and rainy fall/winter/spring. Trees at the site grow new leaves in fall and winter, as rainfall started to arrive in October, which explains why vegetation indices (NDVI, EVI) were higher in October - March than in the summer months. Higher NDVI values in August-September than June-July reflects the large loss (leaf litterfall) of old leaves in August-September.

In short, the seasonal dynamics of vegetation indices at the US-Ho2 and US-NR1 sites are primarily influenced by fluctuations in air temperature, whereas the seasonal dynamics of vegetation indices at the US-Me2 site are predominantly determined by changes in precipitation (water). At the three ENF sites, LSWI maintains positive values over the entire year, which supports the previous forest mapping studies that used LSWI >0 threshold value to identify and map evergreen forests (Zhang et al. 2023).

4.2. Light absorption and gross primary production of evergreen needleleaf forests

The amount of light absorption by chlorophyll in the canopy ($APAR_{chl}$) is calculated as the product of the fraction of light absorption by chlorophyll in the canopy ($FPAR_{chl}$) and the amount of incoming PAR. $FPAR_{chl}$ is estimated as a function of EVI (Liu et al. 2017; Zhang et al. 2018) or SIF (Zhang et al. 2020). In this study for the VPM 3.0, we proposed a new equation to estimate $FPAR_{chl}$ of evergreen needleleaf forests, which is based on the needleleaf structure and chloroplast distribution within a needleleaf (leaf traits). The new equation ($FPAR_{chl}$ = 1.25 x EVI - 0.1) results in higher $FPAR_{chl}$ of evergreen needleleaf forests, which leads to an improved simulation accuracy of GPP_{VPM} at the three ENF sites. Previous research established that the spherically averaged projection area of a needleleaf is precisely one-fourth of its total surface area (Lang 1991; Oker-Blom and Kellomäki 1981; Stenberg 2006). Previous studies and our approach focus on the needle-like

structure of leaves and consider the differences in leaf area between flat leaves and needle leaves, while our method further incorporates the circular distribution of chloroplasts within needle leaves and their decreasing concentration toward the center of the needle. In recent years, substantial progress has been made to estimate canopy-averaged chlorophyll content from time series satellite images, including MODIS images (Croft et al. 2020; Xu et al. 2022), which opens an opportunity to compare $APAR_{chl}$ estimates from these two approaches in the near future.

4.3. Water stress for evergreen needleleaf forests under the Mediterranean climate

The Mediterranean climate is characterized with a wet season and a dry season, and during the dry season water availability is the primary environmental driver of carbon fluxes (Luo et al. 2020). One of the most characteristic traits of plants in Mediterranean ecosystems is the development of deep and extensive root systems, which enable them to absorb water from deeper soil layers (Sardans and Penuelas 2013). Previous studies reported that Ponderosa pine trees at the US-Me2 site have access to additional water from the deep soils in the wet season (Irvine et al. 2004; Thomas et al. 2009). High soil moisture (Fig. 6 g) and vegetation indices (NDVI, EVI, and LSWI) (Fig. 6h) in the wet season (e.g., January – June, October - December) at the site suggest limited or no water stress, too. Based on the previous studies at the US-Me2 site, we assumed $W_{scalar} = 1.0$ during the wet season. During the three-months of dry season (July - September), GPP_{EC} was reduced substantially, indicating the effect of water stress on GPP. In this study we ran the VPM simulations at the US-Me2 site with two different W_{scalar} equations over the dry season ($W_{scalar} = (1+ LSWI) / (1+LSWmax)$) and wet season ($W_{scalar} = 1.0$), which represents how the seasonal dynamics of GPP at the US-Me2 site is affected by water availability over the seasons. The results from the US-Me2 site suggests that the use VPM over other ENF sites in the Mediterranean climates may benefit substantially from (1) evaluating whether trees at those sites have deep roots with access to deep soil water during the wet and dry seasons and (2) assuming $W_{scalar} = 1.0$ in the wet season (no water stress).

A study in Mediterranean climate ecosystems in Spain used meteorological data instead of vegetation indices to construct water stress on GPP and obtained similar results to ours. It found no water stress during the wet season and some stress during the dry season, enhancing the accuracy of GPP simulations (Gilabert et al. 2015). Another study on pine trees in the Mediterranean climate calculated a water availability factor using two-month accumulations of daily rainfall and evapotranspiration (ET). This approach improved modeled GPP by addressing its underestimation during the wet season under the assumption of no water limitations and addressing its overestimation during the dry season by incorporating water limitations (Helman et al. 2017). These studies collectively demonstrate the importance of distinguishing between wet seasons (limited or no water stress) and dry seasons (substantial water stress) in Mediterranean climate ecosystems for improving GPP simulation accuracy, aligning with the findings of our study. Our use of LSWI produced results similar to those reported in studies using meteorological data, demonstrating that remote sensing indices can also effectively estimate water stress under the Mediterranean climate. In the future, meteorological data can complement remote sensing indices like LSWI by helping identify wet and dry seasons, while satellite-based indices can provide detailed spatial and temporal estimates of varying levels of water stress, further enhancing the applicability of our approach.

5. Conclusion

This study analyzed the seasonal dynamics of climate, vegetation indices and carbon fluxes at three evergreen needleleaf forest sites with three types of climates (near coastal area, high mountain area, and Mediterranean climate area). At the US-Ho2 and US-NR1 sites, the seasonal dynamics of radiation, air temperature are synchronous with that of precipitation, and vegetation indices and carbon fluxes are primarily influenced by air temperature. At the US-Me2 site, the seasonal dynamics of radiation, air temperature are asynchronous with that of precipitation, and there are clearly a wet season and a dry season. The seasonal dynamics of vegetation indices and carbon fluxes are largely driven by water availability, including both rainfall and water in deep soils.

This study improved and evaluated the performance of the VPM (v3.0) for evergreen needleleaf forests. The new equation ($FPAR_{chl} = 1.25$ x EVI - 0.1) for estimating $FPAR_{chl}$ incorporates needleleaf traits (leaf shape and chlorophyll distribution), which leads to improving GPP estimation for ENF. As ENF are extensive in the world, incorporating new $FPAR_{chl}$ equation for ENF could lead to further improving estimation of light absorption by chlorophyll and GPP for ENF in the world. At the US-Me2 site, we adjusted W_{scalar} in VPM simulations to reflect deep soil water availability during the wet season. Our results suggest that for ENF with the Mediterranean climate, it is important to gather additional information on whether trees have access to deep soil water or not in the wet season. In those situations where trees have access to deep soil water in the wet season, assuming $W_{scalar} = 1.0$ during the wet season could lead to improving model accuracy of GPP estimates. The results from these ENF sites lay out a foundation for us to use the VPM v3.0, MODIS images, and ERA5 climate data for estimating GPP of evergreen needleleaf forests under diverse climate conditions over large spatial domain.

CRediT authorship contribution statement

Baihong Pan: Writing – review & editing, Writing – original draft, Visualization, Validation, Software, Methodology, Conceptualization. **Xiangming Xiao:** Writing – review & editing, Supervision, Project administration, Methodology, Funding acquisition, Conceptualization. **Li Pan:** Writing – review & editing, Methodology. **Cheng Meng:** Writing – review & editing. **Peter D. Blanken:** Writing – review & editing. **Sean P. Burns:** Writing – review & editing, Data curation. **Jorge A. Celis:** Writing – review & editing. **Chenchen Zhang:** Writing – review & editing. **Yuanwei Qin:** Writing – review & editing.

Declaration of competing interest

The authors declare that they have no known competing financial interests or personal relationships that could have appeared to influence the work reported in this paper.

Acknowledgements

This study was supported in part by research grants from the U.S. National Science Foundation (OIA-1946093) and NASA (80NSSC24K0118). We thank the reviewers for their review and comments for earlier version of the manuscript.

Supplementary materials

Supplementary material associated with this article can be found, in the online version, at doi:10.1016/j.agrformet.2025.110526.

Data availability

Data will be made available on request.

References

Badgley, G., Anderegg, L.D.L., Berry, J.A., Field, C.B., 2019. Terrestrial gross primary production: using NIR(V) to scale from site to globe. Glob. Change Biol. 25, 3731–3740.

Baldocchi, D.D., 2020. How eddy covariance flux measurements have contributed to our understanding of global change biology. Glob. Change Biol. 26, 242–260.

Burns, S.P., Blanken, P.D., Turnipseed, A.A., Hu, J., Monson, R.K., 2015. The influence of warm-season precipitation on the diel cycle of the surface energy balance and carbon dioxide at a Colorado subalpine forest site. Biogeosciences 12, 7349–7377.

Cao, S., Sanchez-Azofeifa, G.A., Duran, S.M., Calvo-Rodriguez, S., 2016. Estimation of aboveground net primary productivity in secondary tropical dry forests using the Carnegie–Ames–Stanford approach (CASA) model. Environ. Res. Lett. 11.

Chang, Q., Xiao, X., Doughty, R., Wu, X., Jiao, W., Qin, Y., 2021. Assessing variability of optimum air temperature for photosynthesis across site-years, sites and biomes and their effects on photosynthesis estimation. Agric. For. Meteorol. 298–299.

Chang, Q., Xiao, X., Jiao, W., Wu, X., Doughty, R., Wang, J., Du, L., Zou, Z., Qin, Y., 2019. Assessing consistency of spring phenology of snow-covered forests as estimated by vegetation indices, gross primary production, and solar-induced chlorophyll fluorescence. Agric. For. Meteorol. 275, 305–316.

Chang, Q., Xiao, X., Wu, X., Doughty, R., Jiao, W., Bajgain, R., Qin, Y., Wang, J., 2020. Estimating site-specific optimum air temperature and assessing its effect on the photosynthesis of grasslands in mid- to high-latitudes. Environ. Res. Lett. 15.

Chu, H., Luo, X., Ouyang, Z., Chan, W.S., Dengel, S., Biraud, S.C., Torn, M.S., Metzger, S., Kumar, J., Arain, M.A., Arkebauer, T.J., Baldocchi, D., Bernacchi, C., Billesbach, D., Black, T.A., Blanken, P.D., Bohrer, G., Bracho, R., Brown, S., Brunsell, N.A., Chen, J., Chen, X., Clark, K., Desai, A.R., Duman, T., Durden, D., Fares, S., Forbrich, I., Gamon, J.A., Gough, C.M., Griffis, T., Helbig, M., Hollinger, D., Humphreys, E., Ikawa, H., Iwata, H., Ju, Y., Knowles, J.F., Knox, S.H., Kobayashi, H., Kolb, T., Law, B., Lee, X., Litvak, M., Liu, H., Munger, J.W., Noormets, A., Novick, K., Oberbauer, S.F., Oechel, W., Oikawa, P., Papuga, S.A., Pendall, E., Prajapati, P., Prueger, J., Quinton, W.L., Richardson, A.D., Russell, E.S., Scott, R.L., Starr, G., Staebler, R., Stoy, P.C., Stuart-Haëntjens, E., Sonnentag, O., Sullivan, R.C., Suyker, A., Ueyama, M., Vargas, R., Wood, J.D., Zona, D., 2021. Representativeness of Eddy-Covariance flux footprints for areas surrounding AmeriFlux sites. Agric. For. Meteorol. 301–302.

Croft, H., Chen, J.M., Wang, R., Mo, G., Luo, S., Luo, X., He, L., Gonsamo, A., Arabian, J., Zhang, Y., Simic-Milas, A., Noland, T.L., He, Y., Homolová, L., Malenovský, Z., Yi, Q., Beringer, J., Amiri, R., Hutley, L., Arellano, P., Stahl, C., Bonal, D., 2020. The global distribution of leaf chlorophyll content. Remote Sens. Environ. 236.

Davidson, E.A., Richardson, A.D., Savage, K.E., Hollinger, D.Y., 2006. A distinct seasonal pattern of the ratio of soil respiration to total ecosystem respiration in a spruce-dominated forest. Glob. Change Biol. 12, 230–239.

Dye, D.G., 2004. Spectral composition and quanta-to-energy ratio of diffuse photosynthetically active radiation under diverse cloud conditions. J. Geophys. Res. Atmos. 109.

Gamon, J.A., Huemmrich, K.F., Wong, C.Y., Ensminger, I., Garrity, S., Hollinger, D.Y., Noormets, A., Penuelas, J., 2016. A remotely sensed pigment index reveals photosynthetic phenology in evergreen conifers. Proc. Natl. Acad. Sci. U. S. A. 113, 13087–13092.

Gamon, J.A., Peñuelas, J., Field, C.B., 1992. A narrow-waveband spectral index that tracks diurnal changes in photosynthetic efficiency. Remote Sens. Environ. 41, 35–44.

Gilabert, M.A., Moreno, A., Maselli, F., Martínez, B., Chiesi, M., Sánchez-Ruiz, S., García-Haro, F.J., Pérez-Hoyos, A., Campos-Taberner, M., Pérez-Priego, O., Serrano-Ortiz, P., Carrara, A., 2015. Daily GPP estimates in Mediterranean ecosystems by combining remote sensing and meteorological data. ISPRS J. Photogramm. Remote Sens. 102, 184–197.

Green, J.K., Seneviratne, S.I., Berg, A.M., Findell, K.L., Hagemann, S., Lawrence, D.M., Gentine, P., 2019. Large influence of soil moisture on long-term terrestrial carbon uptake. Nature 565, 476–479.

Gu, L., Hanson, P.J., Post, W.M., Kaiser, D.P., Yang, B., Nemani, R., Pallardy, S.G., Meyers, T., 2008. The 2007 eastern US spring freeze: increased cold damage in a warming world? Bioscience 58, 253–262.

Havranek, W.M., Tranquillini, W., 1995. 5 - Physiological processes during winter dormancy and their ecological significance. W.K. Smith, & T.M. Hinckley (Eds.). Ecophysiology of Coniferous Forests. Academic Press, San Diego, pp. 95–124.

Helman, D., Lensky, I.M., Osem, Y., Rohatyn, S., Rotenberg, E., Yakir, D., 2017. A biophysical approach using water deficit factor for daily estimations of evapotranspiration and CO₂ uptake in Mediterranean environments. Biogeosciences 14, 3909–3926.

Huang, X., Xiao, J., Ma, M., 2019. Evaluating the performance of satellite-derived vegetation indices for estimating gross primary productivity using FLUXNET observations across the globe. Remote Sens. 11 (Basel).

Huang, X., Xiao, J., Wang, X., Ma, M., 2021. Improving the global MODIS GPP model by optimizing parameters with FLUXNET data. Agric. For. Meteorol. 300.

Huete, A., Didan, K., Miura, T., Rodriguez, E.P., Gao, X., Ferreira, L.G., 2002. Overview of the radiometric and biophysical performance of the MODIS vegetation indices. Remote Sens. Environ. 83, 195–213.

Irvine, J., Law, B., Kurpius, M., Anthoni, P., Moore, D., Schwarz, P., 2004. Age-related changes in ecosystem structure and function and effects on water and carbon exchange in ponderosa pine. Tree Physiol. 24, 753–763.

Jung, M., Schwalm, C., Migliavacca, M., Walther, S., Camps-Valls, G., Koirala, S., Anthoni, P., Besnard, S., Bodesheim, P., Carvalhais, N., Chevallier, F., Gans, F., Goll, D.S., Haverd, V., Köhler, P., Ichii, K., Jain, A.K., Liu, J., Lombardozzi, D., Nabel, J.E.M.S., Nelson, J.A., O'Sullivan, M., Pallandt, M., Papale, D., Peters, W., Pongratz, J., Rödenbeck, C., Sitch, S., Tramontana, G., Walker, A., Weber, U., Reichstein, M., 2020. Scaling carbon fluxes from eddy covariance sites to globe: synthesis and evaluation of the FLUXCOM approach. Biogeosciences 17, 1343–1365.

Junttila, S., Ardö, J., Cai, Z., Jin, H., Kljun, N., Klemedtsson, L., Krasnova, A., Lange, H., Lindroth, A., Mölder, M., Noe, S.M., Tagesson, T., Vestin, P., Weslien, P., Eklundh, L., 2023. Estimating local-scale forest GPP in Northern Europe using Sentinel-2: model comparisons with LUE, APAR, the plant phenology index, and a light response function. Sci. Remote Sens. 7.

Keenan, R.J., Reams, G.A., Achard, F., de Freitas, J.V., Grainger, A., Lindquist, E., 2015. Dynamics of global forest area: results from the FAO global forest resources assessment 2015. For. Ecol. Manage 352, 9–20.

Kim, J., Ryu, Y., Dechant, B., Lee, H., Kim, H.S., Kornfeld, A., Berry, J.A., 2021. Solar-induced chlorophyll fluorescence is non-linearly related to canopy photosynthesis in a temperate evergreen needleleaf forest during the fall transition. Remote Sens. Environ. 258.

Knowles, J.F., Scott, R.L., Biederman, J.A., Blanken, P.D., Burns, S.P., Dore, S., Kolb, T.E., Litvak, M.E., Barron-Gafford, G.A., 2020. Montane forest productivity across a semiarid climatic gradient. Glob. Change Biol. 26, 6945–6958.

Knutti, R., Rugenstein, M.A.A., Hegerl, G.C., 2017. Beyond equilibrium climate sensitivity. Nat. Geosci. 10, 727–736.

Korner, C., Mohl, P., Hiltbrunner, E., 2023. Four ways to define the growing season. Ecol. Lett. 26, 1277–1292.

Lang, A.R.G., 1991. Application of some of Cauchy's theorems to estimation of surface areas of leaves, needles and branches of plants, and light transmittance. Agric. For. Meteorol. 55, 191–212.

Lasslop, G., Reichstein, M., Papale, D., Richardson, A.D., Arneth, A., Barr, A., Stoy, P., Wohlfahrt, G., 2009. Separation of net ecosystem exchange into assimilation and respiration using a light response curve approach: critical issues and global evaluation. Glob. Change Biol. 16, 187–208.

Law, B., 2022. AmeriFlux FLUXNET-1F US-Me2 Metolius mature Ponderosa Pine. Lawrence Berkeley National Lab.(LBNL), Berkeley, CA (United States).

Law, B.E., Van Tuyl, S., Cescatti, A., Baldocchi, D.D., 2001. Estimation of leaf area index in open-canopy ponderosa pine forests at different successional stages and management regimes in Oregon. Agric. For. Meteorol. 108, 1–14.

Liu, Y., Wu, C., Peng, D., Xu, S., Gonsamo, A., Jassal, R.S., Altaf Arain, M., Lu, L., Fang, B., Chen, J.M., 2016. Improved modeling of land surface phenology using MODIS land surface reflectance and temperature at evergreen needleleaf forests of central North America. Remote Sens. Environ. 176, 152–162.

Liu, Z., Wu, C., Peng, D., Wang, S., Gonsamo, A., Fang, B., Yuan, W., 2017. Improved modeling of gross primary production from a better representation of photosynthetic components in vegetation canopy. Agric. For. Meteorol. 233, 222–234.

Luo, Y., El-Madany, T., Ma, X., Nair, R., Jung, M., Weber, U., Filippa, G., Bucher, S.F., Moreno, G., Cremonese, E., Carrara, A., Gonzalez-Cascon, R., Caceres Escudero, Y., Galvagno, M., Pacheco-Labrador, J., Martin, M.P., Perez-Priego, O., Reichstein, M., Richardson, A.D., Menzel, A., Romermann, C., Migliavacca, M., 2020. Nutrients and water availability constrain the seasonality of vegetation activity in a Mediterranean ecosystem. Glob. Change Biol. 26, 4379–4400.

Ma, X., Huete, A., Yu, Q., Restrepo-Coupe, N., Beringer, J., Hutley, L.B., Kanniah, K.D., Cleverly, J., Eamus, D., 2014. Parameterization of an ecosystem light-use-efficiency model for predicting savanna GPP using MODIS EVI. Remote Sens. Environ. 154, 253–271.

Meek, D., Hatfield, J., Howell, T., Idso, S., Reginato, R., 1984. A generalized relationship between photosynthetically active radiation and solar radiation 1. Agron. J. 76, 939–945.

Mohammed, G.H., Colombo, R., Middleton, E.M., Rascher, U., van der Tol, C., Nedbal, L., Goulas, Y., Perez-Priego, O., Damm, A., Meroni, M., Joiner, J., Cogliati, S., Verhoef, W., Malenovsky, Z., Gastellu-Etchegorry, J.P., Miller, J.R., Guanter, L., Moreno, J., Moya, I., Berry, J.A., Frankenberg, C., Zarco-Tejada, P.J., 2019. Remote sensing of solar-induced chlorophyll fluorescence (SIF) in vegetation: 50 years of progress. Remote Sens. Environ. 231.

Monteith, J.L., 1972. Solar radiation and productivity in tropical ecosystems. J. Appl. Ecol. 9, 747.

Muñoz-Sabater, J., Dutra, E., Agustí-Panareda, A., Albergel, C., Arduini, G., Balsamo, G., Boussetta, S., Choulga, M., Harrigan, S., Hersbach, H., Martens, B., Miralles, D.G., Piles, M., Rodríguez-Fernández, N.J., Zsoter, E., Buontempo, C., Thépaut, J.N., 2021. ERA5-Land: a state-of-the-art global reanalysis dataset for land applications. Earth Syst. Sci. Data 13, 4349–4383.

Muñoz Sabater, J. (2019). ERA5-Land hourly data from 1981 to present. Copernicus climate change service (C3S) climate data store (CDS), 10.

Ogle, K., Lucas, R.W., Bentley, L.P., Cable, J.M., Barron-Gafford, G.A., Griffith, A., Ignace, D., Jenerette, G.D., Tyler, A., Huxman, T.E., Loik, M.E., Smith, S.D., Tissue, D.T., 2012. Differential daytime and night-time stomatal behavior in plants from North American deserts. New Phytol. 194, 464–476.

Oker-Blom, P., Kellomäki, S., 1981. Light regime and photosynthetic production in the canopy of a scots pine stand during a prolonged period. Agric. Meteorol. 24, 185–199.

Pan, L., Xiao, X., Pan, B., Meng, C., Staebler, R.M., Zhang, C., Qin, Y., 2024a. Interannual variations and trends of gross primary production and transpiration of four mature deciduous broadleaf forest sites during 2000–2020. Remote Sens. Environ. 304.

Pan, L., Xiao, X., Yao, Y., Pan, B., Yin, C., Meng, C., Qin, Y., Zhang, C., 2024b. Site-specific apparent optimum air temperature for vegetation photosynthesis across the globe. Sci. Data 11, 758.

Pei, Y., Dong, J., Zhang, Y., Yuan, W., Doughty, R., Yang, J., Zhou, D., Zhang, L., Xiao, X., 2022. Evolution of light use efficiency models: improvement, uncertainties, and implications. Agric. For. Meteorol. 317.

Pierrat, Z., Magney, T., Parazoo, N.C., Grossmann, K., Bowling, D.R., Seibt, U., Johnson, B., Helgason, W., Barr, A., Bortnik, J., Norton, A., Maguire, A., Frankenberg, C., Stutz, J., 2022. Diurnal and seasonal dynamics of solar-induced chlorophyll fluorescence, vegetation indices, and gross primary productivity in the boreal forest. J. Geophys. Res.: Biogeosciences 127.

Potter, C.S., Randerson, J.T., Field, C.B., Matson, P.A., Vitousek, P.M., Mooney, H.A., Klooster, S.A., 1993. Terrestrial ecosystem production: a process model based on global satellite and surface data. Glob. Biogeochem. Cycles 7, 811–841.

Richardson, A.D., Hollinger, D.Y., Shoemaker, J.K., Hughes, H., Savage, K., Davidson, E. A., 2019. Six years of ecosystem-atmosphere greenhouse gas fluxes measured in a sub-boreal forest. Sci. Data 6, 117.

Running, S.W., & Zhao, M. (2015). Daily GPP and annual NPP (MOD17A2/A3) products NASA earth observing system MODIS land algorithm. MOD17 User's Guide, 2015, 1–28.

Sardans, J., Penuelas, J., 2013. Plant-soil interactions in Mediterranean forest and shrublands: impacts of climatic change. Plant Soil 365, 1–33.

Smallman, T.L., Williams, M., 2019. Description and validation of an intermediate complexity model for ecosystem photosynthesis and evapotranspiration: aCM-GPP-ETv1. Geosci. Model. Dev. 12, 2227–2253.

Stenberg, P., 2006. A note on the G-function for needle leaf canopies. Agric. For. Meteorol. 136, 76–79.

Still, C.J., Rastogi, B., Page, G.F.M., Griffith, D.M., Sibley, A., Schulze, M., Hawkins, L., Pau, S., Detto, M., Helliker, B.R., 2021. Imaging canopy temperature: shedding (thermal) light on ecosystem processes. New Phytol. 230, 1746–1753.

Thomas, C.K., Law, B.E., Irvine, J., Martin, J.G., Pettijohn, J.C., Davis, K.J., 2009. Seasonal hydrology explains interannual and seasonal variation in carbon and water exchange in a semiarid mature ponderosa pine forest in central Oregon. J. Geophys. Res. 114.

Trueba, S., Theroux-Rancourt, G., Earles, J.M., Buckley, T.N., Love, D., Johnson, D.M., Brodersen, C., 2022. The three-dimensional construction of leaves is coordinated with water use efficiency in conifers. New Phytol. 233, 851–861.

Tucker, C.J., 1979. Red and photographic infrared linear combinations for monitoring vegetation. Remote Sens. Environ. 8, 127–150.

Urraca, R., Huld, T., Gracia-Amillo, A., Martinez-de-Pison, F.J., Kaspar, F., Sanz-Garcia, A., 2018. Evaluation of global horizontal irradiance estimates from ERA5 and COSMO-REA6 reanalyses using ground and satellite-based data. Sol. Energy 164, 339–354.

Vermote, E. (2015). MOD09A1 MODIS/terra surface reflectance 8-day L3 global 500m SIN grid V006. (No Title).

Vinukollu, R.K., Wood, E.F., Ferguson, C.R., Fisher, J.B., 2011. Global estimates of evapotranspiration for climate studies using multi-sensor remote sensing data: evaluation of three process-based approaches. Remote Sens. Environ. 115, 801–823.

Wagle, P., Xiao, X., Kolb, T.E., Law, B.E., Wharton, S., Monson, R.K., Chen, J., Blanken, P. D., Novick, K.A., Dore, S., Noormets, A., Gowda, P.H., 2016. Differential responses of carbon and water vapor fluxes to climate among evergreen needleleaf forests in the USA. Ecol. Process. 5.

Wang, J., Xiao, X., Wagle, P., Ma, S., Baldocchi, D., Carrara, A., Zhang, Y., Dong, J., Qin, Y., 2016. Canopy and climate controls of gross primary production of Mediterranean-type deciduous and evergreen oak savannas. Agric. For. Meteorol. 226 (227), 132–147.

Wang, R., Bowling, D.R., Gamon, J.A., Smith, K.R., Yu, R., Hmimina, G., Ueyama, M., Noormets, A., Kolb, T.E., Richardson, A.D., Bourque, C.P.A., Bracho, R., Blanken, P. D., Black, T.A., Arain, M.A., 2023. Snow-corrected vegetation indices for improved gross primary productivity assessment in North American evergreen forests. Agric. For. Meteorol. 340.

Wong, C.Y.S., D'Odorico, P., Arain, M.A., Ensminger, I., 2020. Tracking the phenology of photosynthesis using carotenoid-sensitive and near-infrared reflectance vegetation indices in a temperate evergreen and mixed deciduous forest. New Phytol. 226, 1682–1695.

Wong, C.Y.S., Gamon, J.A., 2015. Three causes of variation in the photochemical reflectance index (PRI) in evergreen conifers. New Phytol. 206, 187–195.

Xiao, X., 2004. Modeling gross primary production of temperate deciduous broadleaf forest using satellite images and climate data. Remote Sens. Environ. 91, 256–270.

Xiao, X., Boles, S., Liu, J., Zhuang, D., Liu, M., 2002. Characterization of forest types in Northeastern China, using multi-temporal SPOT-4 VEGETATION sensor data. Remote Sens. Environ. 82, 335–348.

Xiao, X., Hollinger, D., Aber, J., Goltz, M., Davidson, E.A., Zhang, Q., Moore, B., 2004. Satellite-based modeling of gross primary production in an evergreen needleleaf forest. Remote Sens. Environ. 89, 519–534.

Xiao, X., Zhang, Q., Hollinger, D., Aber, J., Berrien, A., Iii, M., 2005a. Modeling gross primary production of an evergreen needleleaf forest using MODIS and climate data. Ecol. Appl. 15, 954–969.

Xiao, X., Zhang, Q., Saleska, S., Hutyra, L., De Camargo, P., Wofsy, S., Frolking, S., Boles, S., Keller, M., Moore, B., 2005b. Satellite-based modeling of gross primary production in a seasonally moist tropical evergreen forest. Remote Sens. Environ. 94, 105–122.

Xin, F., Xiao, X., Zhao, B., Miyata, A., Baldocchi, D., Knox, S., Kang, M., Shim, K.M., Min, S., Chen, B., Li, X., Wang, J., Dong, J., Biradar, C., 2017. Modeling gross primary production of paddy rice cropland through analyses of data from CO2 eddy flux tower sites and MODIS images. Remote Sens. Environ. 190, 42–55.

Xu, M., Liu, R., Chen, J.M., Liu, Y., Wolanin, A., Croft, H., He, L., Shang, R., Ju, W., Zhang, Y., He, Y., Wang, R., 2022. A 21-year time series of global leaf chlorophyll content maps from MODIS imagery. IEEE Trans. Geosci. Remote Sens. 60, 1–13.

Yuan, H., Wu, C., Lu, L., Wang, X., 2018. A new algorithm predicting the end of growth at five evergreen conifer forests based on nighttime temperature and the enhanced vegetation index. ISPRS J. Photogramm. Remote Sens. 144, 390–399.

Yuan, W., Liu, S., Zhou, G., Zhou, G., Tieszen, L.L., Baldocchi, D., Bernhofer, C., Gholz, H., Goldstein, A.H., Goulden, M.L., Hollinger, D.Y., Hu, Y., Law, B.E., Stoy, P. C., Vesala, T., Wofsy, S.C., 2007. Deriving a light use efficiency model from eddy covariance flux data for predicting daily gross primary production across biomes. Agric. For. Meteorol. 143, 189–207.

Zeng, J., Matsunaga, T., Tan, Z.H., Saigusa, N., Shirai, T., Tang, Y., Peng, S., Fukuda, Y., 2020. Global terrestrial carbon fluxes of 1999-2019 estimated by upscaling eddy covariance data with a random forest. Sci. Data 7, 313.

Zeng, Y., Hao, D., Huete, A., Dechant, B., Berry, J., Chen, J.M., Joiner, J., Frankenberg, C., Bond-Lamberty, B., Ryu, Y., Xiao, J., Asrar, G.R., Chen, M., 2022. Optical vegetation indices for monitoring terrestrial ecosystems globally. Nat. Rev. Earth Environ. 3, 477–493.

Zhang, C., Xiao, X., Zhao, L., Qin, Y., Doughty, R., Wang, X., Dong, J., Yang, X., 2023. Mapping eucalyptus plantation in Guangxi, China by using knowledge-based algorithms and PALSAR-2, Sentinel-2, and Landsat images in 2020. Int. J. Appl. Earth Obs. Geoinf. 120.

Zhang, Q., Xiao, X., Braswell, B., Linder, E., Baret, F., Mooreiii, B., 2005. Estimating light absorption by chlorophyll, leaf and canopy in a deciduous broadleaf forest using MODIS data and a radiative transfer model. Remote Sens. Environ. 99, 357–371.

Zhang, Q., Xiao, X., Braswell, B., Linder, E., Ollinger, S., Smith, M.L., Jenkins, J.P., Baret, F., Richardson, A.D., Moore, B., Minocha, R., 2006. Characterization of seasonal variation of forest canopy in a temperate deciduous broadleaf forest, using daily MODIS data. Remote Sens. Environ. 105, 189–203.

Zhang, Y., Xiao, X., Jin, C., Dong, J., Zhou, S., Wagle, P., Joiner, J., Guanter, L., Zhang, Y., Zhang, G., Qin, Y., Wang, J., Moore, B., 2016. Consistency between sun-induced chlorophyll fluorescence and gross primary production of vegetation in North America. Remote Sens. Environ. 183, 154–169.

Zhang, Y., Xiao, X., Wolf, S., Wu, J., Wu, X., Gioli, B., Wohlfahrt, G., Cescatti, A., van der Tol, C., Zhou, S., Gough, C.M., Gentine, P., Zhang, Y., Steinbrecher, R., Ardö, J., 2018. Spatio-temporal convergence of maximum daily light-use efficiency based on radiation absorption by canopy chlorophyll. Geophys. Res. Lett. 45, 3508–3519.

Zhang, Y., Xiao, X., Wu, X., Zhou, S., Zhang, G., Qin, Y., Dong, J., 2017. A global moderate resolution dataset of gross primary production of vegetation for 2000-2016. Sci. Data 4, 170165.

Zhang, Z., Zhang, Y., Zhang, Y., Gobron, N., Frankenberg, C., Wang, S., Li, Z., 2020. The potential of satellite FPAR product for GPP estimation: an indirect evaluation using solar-induced chlorophyll fluorescence. Remote Sens. Environ. 240.

Zheng, Y., Shen, R., Wang, Y., Li, X., Liu, S., Liang, S., Chen, J.M., Ju, W., Zhang, L., Yuan, W., 2020. Improved estimate of global gross primary production for reproducing its long-term variation, 1982–2017. Earth Syst. Sci. Data 12, 2725–2746.